Attosecond X-ray absorption fine-structure spectroscopy in condensed matter

by

Bárbara Buades

Thesis Advisor:
Prof. Dr. Jens Biegert

A thesis submitted in fulfillment of the requirements
for the degree of Doctor of Philosophy
in the

Attoscience and Ultrafast Optics

ICFO – Institut de Ciències Fotòniques
UPC – Universitat Politècnica de Catalunya

Barcelona, June 2018

Thesis committee:

Prof. Dr. Rosario González Férez (University of Granada, Spain)
Dr. Eric Pellegrin (CELLS-ALBA Synchrotron Light Source, Spain)
Prof. Dr. Javier García de Abajo (ICFO – Institut de Ciències Fotòniques, Spain)

Abstract

Attoscience aims to study electron dynamics in matter with unprecedented temporal resolution by using the shortest human-made pulses. Currently, such resolution is only provided by sources that deliver attosecond pulses based on the high-harmonic generation (HHG) process. In this thesis we make use of the demonstration of the generation of isolated attosecond pulses in the soft X-ray (SXR) regime covering the entire water window (284 eV to 543 eV) with pulse durations shorter than 300 as. Such a source is used to explore its own development, the spectroscopic capabilities of the pulses as well as the spectroscopic differences from existing X-ray sources, and finally to exploit the potential of the provided extraordinary temporal resolution. These capabilities lead to three main experimental findings presented in this thesis that provide insights into chemical and physical processes that occur on the attosecond timescale.

We report on the ability to spectrally tune our source 150 eV across the water window by controlling the pressure during the HHG process and the HHG target position with respect to the focal plane of the driving laser pulse. We associate the changes in pressure and target position with a phase matching change between the driving laser pulse of the HHG process and the generated SXR radiation that is mainly caused by a change in the ionisation fraction. These phase matching changes are also compared to a carrier-to-envelope phase changes of the driving laser field.

The attosecond SXR source is used for X-ray absorption fine structure (XAFS) spectroscopy. Our XAFS studies enable the simultaneous probing of extended XAFS (EXFAS) and near edge XAFS (NEXAFS) in graphite, providing element specificity and orbital sensitivity with identification of the σ^* and π^* orbitals in synchronicity with the material's four characteristic bonding distances. This illustrates the potential capability of correlating electron dynamics with structural dynamics with attosecond resolution being able to resolve charge migration, electron-phonon coupling and structural transitions. Our XAFS investigations also reveal spectral changes in graphite and TiS_2 as a consequence of the shorter attosecond pulse compared to the longer picosecond pulse that are typically used in synchrotron facilities. An extended theory is still required to link Auger electron spectroscopy,

total electron yield and XAFS using synchrotron radiation with attoXAFS to decouple the different electron dynamics involved on each of the measurements.

Finally, the attosecond pulses are employed to interrogate charge dynamics with unprecedented temporal resolution inside a compound quasi-2D material, TiS_2. By synchronising a 1.85 μm pump pulse with the probing attosecond SXR pulse, we observe that the shape of the X-ray absorption line changes from a Lorentzian distribution to a Fano-type distribution oscillating with twice the pump electric field frequency. The absorption changes appear due to an acquired dipole phase response of the photo-excited core-level electron induced by the consecutive arrival of the infrared pump pulse. This demonstrates that field-driven intra-band dynamics dominate over inter-band dynamics. Sub-cycle laser-induced electron dynamics are successfully resolved due to the fast decay of the core-level electron excitation within a few femtoseconds. SXR radiation also provides element specificity of attoXAFS which permits, in combination with theory, the visualisation of the flow of charge amongst the atoms inside the unit cell in real time. The combined spatio-temporal capabilities of attosecond transient XAFS may prove decisive to investigate the correlated motion of carriers in quantum materials such as phase-transitions and superconductors.

Acknowledgements

I would like to thank Prof. Dr. Jens Biegert for giving me the opportunity to join his group for my PhD and also for his guidance during this tough, intense and rewarding journey. In particular, I appreciate his support during long days, nights, weeks and months of continuous measurement campaigns and his unstoppable motivation and belief in the experimental results. I also feel privileged for the numerous international and national conferences he encouraged me to go to and present our work. I thank Jens for showing his trust and faith in letting me decide, plan and lead the accomplished experimental results.

The achievements of this thesis should also be attributed to the help of others. Prof. Antonio Picón, Dr. Seth L. Cousin, Dr. Dane R. Austin, Dr. Iker León, Dr. Judith Dura, Dr. Stephan M. Teichmann, Dr. Francisco Silva, Dr. Matthias Baudisch, Dr. Noslen Suárez, Dr. Idoia Martí, Dr. Michael Pullen, Peter Schmidt and Daniel Sánchez have contributed with both scientific and personal support who became mentors and friends for me. Dr. Caterina Cocchi, Prof. Claudia Draxl, Prof. Simon Wall, Dr. Fausto Sirotti, Prof. John J. Rehr, Dr. Azzedine Bendounan, Dr. Arnaud Couairon, Dr. Dooshaye Moonshiram, Samuel Mañas-Valero, Dr. Thomas Danz, Prof. Kazuhiro Yabana, Dr. Mitsuharu Uemoto and Dr. Martin Schultze have given us collaborative scientific support on the data analysis and understanding of the results.

I also want to thank the AUO group members who made everyday a great working environment. Thanks to Nicola Di Palo, Dr. Kasra Amini, Julius Huijts, Ugaitz Elu, Aurelien Sanchez, Dr. Benjamin Wolter, Dr. Daniel Rivas, Dr. Themistoklis P. H. Sidiropoulos, Dr. Tobias Steinle, Irina Pi, Sergio Hilario, Stefano Severino, Xinyao Liu, Dr. Michele Sclafan, Dr. Ioachim Pupeza, Dr. Michäel Hemmer, Dr. Alexander Grün, Dr. Philip K. Bates, Dr. Olivier Chalus, Prof. Tsuneto Kanai, Vittorio Di Pietro, Dr. Lenard Vamos, Dr. Hugo Pires, Alexandre Thai, Dr. Alexander Britz.

A special thanks to the unconditional support and love I have received from my friends no matter where we are: Núria, Clara C., Maria, Luci, Gemma, Ian, Albert, Marc, Edu, Arnau, Tomeu, Mario, Clara B., Cristina, Oscar, Genís, Alberto, Xavi, Poy, Misk, Elena, Rita, Eloi, Ivan G., Marieke, Chiara, Marina M. To the

people that made Barcelona a great place to live in and showed me around: Simon, Achim, James, Juan M., Miriam, Kevin, Nico, Gabi, Roland, Lisa, Sarah, Oller, Alba, Rafa, Arturo, Ana, Carlos, Thomas, Alex, Laura, Jianbo, Mussie, Anjana, Isa, Pau B., Diego, Pau G., Marina, Mònica, Bernardo, Chetan, Ivan N., Jessica, Alessandro, Eric, Fabien, Antoine and Maite.

To my family, who have always been a big pillar of my life showing me the positive sides of the difficult moments.

Contents

Introduction

Access to attosecond time dynamics is now available. Since the generation of the first pulses with sub-femtosecond pulse durations in 2002[1] a large number of experiments have been performed to investigate electron dynamics in atoms[1–9], molecules[10–13] and solids[14–21] with unprecedented temporal resolution. Attosecond pulses are obtained via high harmonic generation (HHG)[22,23] which can be explained with the three-step model: 1) A laser pulse with sufficiently high intensity can promote an electron into the continuum via tunnel ionisation. 2) The liberated electron is accelerated away by the electric field. At the change of sign of the oscillating electric field the electron is then accelerated back to the parent ion, acquiring a large kinetic energy. 3) The electron may recombine with the parent ion releasing the access of kinetic energy emitting a photon of high energy. This process occurs during a fraction of the driving laser field period, hence leading to the emission of a short bursts of radiation. Contributions from each wave cycle within a multi-cycle driving laser pulse result in the generation of trains of attosecond pulses[24]. Upon restricting these bursts to within one-half cycle of the laser field, a single attosecond or femtosecond pulse may be isolated[25], essential for performing time-resolved experiments in order to investigate the electron dynamics and understand the underlying mechanism of the first steps of any physical process and chemical reaction.

The first-generation of attosecond light sources were driven by pulses from Ti:Sapphire laser with a central wavelength, λ_L, of 800 nm. Those sources provided attosecond pulses at centre photon energy up to only 100 eV with a bandwidth of a few tens of eV[25–27]. Further up-scaling of central photon energies required the development of novel laser sources at the mid-IR wavelengths[28,29]. This is easy to understand within the three-step model. The period of longer-wavelength driving lasers gives an ionised electron more time to be accelerated in the continuum, and to acquire a higher kinetic energy before recombining with its parent ion, thus that leads to higher photon energies. Following this strategy, recent developments have been reported with schemes that reached photon energies up to 350 eV, covering the carbon K-shell edge at 284 eV demonstrating the shortest world record pulse duration of 53 as[30] which was beaten later for the generation of attosecond pulses with 43 as pulse duration but with photon energies below 190 eV[31].

However, wavelength-scaling of the HHG process leads to a tremendous decrease of efficiency scaled by the power of $\lambda_L^{-(5-9)}$ from wavelengths in the visible to around 2 μm[32–35]. To ensure high HHG photon flux at longer driving laser wavelengths the radiation from the emitter along the HHG target needs to be phase matched coherently. The generated spectral shape of the attosecond pulses is highly dependent on the phase and amplitude of the driving laser. This represents one of the main difficulties for spectroscopic applications, as the measurements require a high stability on the carrier envelope phase (CEP) of the driving laser[36].

To probe electron dynamics induced by laser pulses, a pump (inducing) pulse needs to be synchronised with the attosecond probe pulse with a controlled time delay, ideally with attosecond temporal resolution. The pump pulse induces electron dynamics that can be probed by the attosecond pulses using spectroscopic techniques. To distinguish the character of electron dynamics inside composed materials element specificity is required to be added in attosecond transient experiments. Element specificity can be provided by spectroscopic techniques such as X-ray absorption fine structure (XAFS) spectroscopy which is a well-established technique implemented at synchrotron and free-electron laser facilities despite of lacking attosecond temporal resolution[37,38]. An inner core shell electron is excited from a well localised state to an unoccupied state in the conduction band or in the continuum by following selection rules leading to element and orbital specificity. This technique requires photon energies high enough that can access inner core shells of different elements. Recently, we have demonstrated the extension of attosecond pulses to cover higher photon energies into a spectral region of special interest, which extends from 284 eV to 543 eV, known as the water window[39–41]. This spectral range is very attractive because it covers the K-edge transitions of carbon, nitrogen, and oxygen, three of the four most common elements in biological molecules, with photon energies around 284 eV, 410 eV, and 543 eV, respectively. These pulses provide the ultrafast temporal resolution in combination with sufficient spectral coverage in a photon energy range that accesses core-level transitions, thus offering element specificity.

Outline

This thesis describes first in Chap. 1 the experimental setup where isolated attosecond pulses in the water window are generated and tailored to afterwards be used for XAFS spectroscopic analysis in which a synchronised femtosecond pump laser pulse can be added to probe time-resolved dynamics in solids.

Tailoring of isolated attosecond pulses in the soft-X-ray regime with phase

match control over their generation is described in Chap. 2 as the first result of this thesis. The spectroscopic capabilities of the generated soft X-ray radiation through a XAFS analysis in graphite are introduced in Chap. 3 followed by an experimental comparison of using X-ray radiation confined in either attosecond pulses through HHG or picosecond pulses being this last one from a synchrotron radiation source. This comparison is shown for both graphite and TiS_2 samples. A real-time XAFS spectroscopy investigation in TiS_2 with attosecond resolution is presented in Chap. 4 . Finally, a summary and outlook of the accomplished results are provided.

1 Experimental fundamentals

This chapter shows the experimental setups used to achieve the results described in Chap. 2 (Tailoring attosecond soft X-ray pulses), Chap. 3 (Attosecond X-ray absorption fine-structure spectroscopy) and Chap. 4 (Attosecond transient X-ray absorption fine-structure spectroscopy).

Firstly, in Sec. 1.1 a brief description is given of the driving laser source to generate stable and reproducible isolated attosecond pulses in the soft X-ray (SXR) regime by ponderomotive scaling and temporal gating the HHG process. An additional requirement is a high pulse-to-pulse stability and control over the CEP. Secondly, in Sec. 1.2 the requirements of the beamline for both the generation of high photon flux SXR attosecond pulses and their propagation are presented. This setup is used for XAFS experiments. Section 1.3 outlines the capabilities of adding synchronised femtosecond pump pulses in combination with the attosecond pulses used to perform time-resolved XAFS measurements. Three modified setups used for different pump pulses are explored. Also shown is the method used to find the spatio-temporal overlap between pump and probe pulses within 30 fs of each other. The chapter finishes with a short summary of the setups used.

1.1 Driving laser for HHG

The High harmonic generation (HHG) process can give access to attosecond-duration pulses. Isolated attosecond pulses with stable and spectrally-tunable photon flux in the soft X-ray regime in the water window up to 550 eV that can be used for spectroscopy techniques puts strict constrains on the driving laser pulses. In this section, it is described how the driving laser source is designed to: 1) make use of a ponderomotive scaling HHG process as to achieve such a high photon energy, 2) temporally gate the HHG process as to lead to a single isolated attosecond pulse per driving laser pulse, and 3) spectrally control the generated radiation by controlling the driving laser carrier-to-envelope phase (CEP).

1.1.1 Ponderomotive scaling HHG process

Generating radiation that spans the entire water window requires ponderomotively scaled HHG. This is related here by driving the HHG process with pulses at a central wavelength of $\lambda_L = 1.85$ μm instead of a Ti:Sapphire laser at $\lambda_L = 800$ nm[25–27].

The highest reachable photon energy, the so called cutoff energy (E_{cutoff}), based on the single atom response during the HHG process, is given by

$$E_{cutoff} \approx I_p + 3.17 U_p, \tag{1.1}$$

where I_p is the ionisation potential of the atom used for HHG and U_p is the ponderomotive energy which is the averaged energy of the tunnel-ionised electron that follows the oscillation of the driving electric field, E_0, until it is returned to the parent ion during the HHG process[42]. U_p is given by

$$U_p = \frac{e^2 E_0^2 \lambda_L^2}{16\pi^2 c^2} \tag{1.2}$$

where e is the electron charge and c the speed of light. U_p scales quadratically with the wavelength of the driving laser leading to an extension of the reachable cutoff energy, E_{cutoff}. This approach was already demonstrated in 2001 by B. Shan and Z. Chang[28] and afterwards followed by a number of other groups[28,30,36,43–49]. Another approach is to increase the driving laser intensity while preserving a 800 nm central wavelength from a Ti:Sapphire laser[50–54]. Although higher photon energies have been reached in both which approached the keV regime, no other source has yet been used to demonstrate the generation of isolated attosecond pulses with energies beyond 350 eV.

The realization of the driving laser of the HHG process starts from a lab-built Ti:Sapphire laser at a 1kHz repetition rate, with a pulse energy of 7 mJ and a pulse duration of 40 fs. The Ti:Sapphire output has a near-perfect beam profile and a high intensity stability (below 1%) which is an essential requirement as it is the input for the next component which is a High-Energy TOPAS. The TOPAS is a commercial optical parametric amplifier (OPA) with 3 stages that converts an input pulse with a wavelength of 800 nm to 1.85 μm. Firstly, a small fraction of energy of the 800 nm pulses is used to generate white light up to at 1.3 μm. Then, the first OPA stage amplifies the 1.3 μm in a non-collinear geometry. The amplified 1.3 μm is sent to the second OPA stage which is collinear with the pump to generate an idler of 1.85 μm which is amplified in the last OPA stage in a slightly non-collinear geometry to spatially separate non-desired frequencies. All OPA stages are pumped by replicas of the 800 nm input pulses. The 1.85 μm pulses have an energy of 1 mJ and a pulse duration of 45 fs which can be focused down to a 50 μm beam waist with an intensity of 0.3 PW/cm^2.

The high energy TOPAS output could be used already to generate radiation in the water window via HHG process. However, since these pulses contain multiple cycles ($>$ 7 cycles) using them would lead to the generation of a train of attosecond pulses per driving laser pulse. Section 1.1.2 describes different methods to make isolated attosecond pulses. We use pulse compression of the TOPAS output in a gas-filled hollow-core fiber to temporal gate the HHG process to a single-cycle[55].

1.1.2 Temporal gating

HHG occurs at each half cycle of the driving electric field where its intensity is above the ionisation threshold. Long (or multi-cycle) laser pulses result in an emission of several attosecond bursts within the driving laser pulse leading to the generation of trains of attosecond pulses[24]. Upon restricting these bursts to within one-half cycle of the laser field, a single attosecond pulse may be isolated. This is essential to preserve an attosecond temporal resolution in studies of electron dynamics in pump-probe experiments[56]. Since half-cycle pulses are not manufacturable, and it has not been until recently that single-cycle optical pulses have been demonstrated[57], different experimental techniques have been developed to restrict the efficient generation of an attosecond burst to a single-half-cycle of the driving laser. From multiple-cycle pulses one option is to temporally modulate the ellipticity of the driving pulses to control their linear polarization over a temporal gate. This technique is called polarization gating[58]. At 2 μm an ellipticity of 0.09 is enough to drop the efficiency of the HHG process one order of magnitude[59,60]. A calculation of restricting linear polarization to a single-cycle (6.5 fs at 2 μm)

from the TOPAS output with 45 fs pulse duration yields between 20% and 30% of used energy over the total pulse energy. This technique has been successfully used for 1.6 - 2.1 μm wavelength pulses only with already short few-cycle pulses[30] in order to not to waste pulse energy. Another technique so called double optical gating[61] combines the polarization gating technique with adding a weak second harmonic field to deplete the ground state population leading to a single generation of attosecond pulses each full optical cycle. This technique relaxes temporal gating constrains but introduces more complexity in the HHG process. Other techniques such as amplitude gating[62], spectral gating[63], spatio-temporal gating[64,65] or ionisation gating[66] require few-cycle pulse.

Amplitude gating relies on changing the CEP of a few-cycle pulse to ensure that only one optical cycle with the highest field amplitude contributes to the HHG process. Since different field amplitudes generate burst at different spectral ranges, by using spectral filters or mirrors that highly reflect a certain spectral bandwidth, one can isolate attosecond pulses by combining amplitude gating with spectral gating. The drawbacks of these techniques are the inflexibility of spectral adjustment, the limitation of a short spectral bandwidth limiting the minimum attosecond pulse duration and the lack of the existence of a variety of spectral filters that can be used in the soft X-ray regime[67]. Spatio-temporal gating or using the attosecond lighthouse effect is an alternative technique that consists of modifying the driving pulse with a wavefront rotation in the generation medium from which consecutive attosecond burst will travel in different directions. This technique has also been implemented at 1.85 μm at the expense of cutoff energy (reducing from 400 eV to 300 eV) and also a decrease in the produced photon flux of almost 1 order of magnitude[39]. An ionisation gating or phase matching gating technique needs relatively high intensity driving lasers[66] or a high pressure HHG target[68] which has been successfully demonstrated from multiple-cycle pulses again at the expense of limiting the cutoff energies.

The combination of an ionisation phase matching gating technique applied to a few-cycle pulse has shown efficient generation of isolated attosecond pulses in the extreme ultra-violet (XUV) regime[69]. Here a similar approach is applied to long-wavelength driving laser pulses. A sub-two-cycle driving laser pulse is produced by sending the TOPAS's output into a hollow-core fibre with 400 μm inner diameter that is filled with argon at 1.2 bar. By propagating through the hollow-core fibre, the pulse's spectrum is broadened and its output is compressed using a bulk material (3 mm-thick RG1000) down to 12 fs[55,70]. Figure 1.1 shows the broadband infrared spectrum output of the hollow-core fibre with a central wavelength of 1.85 μm.

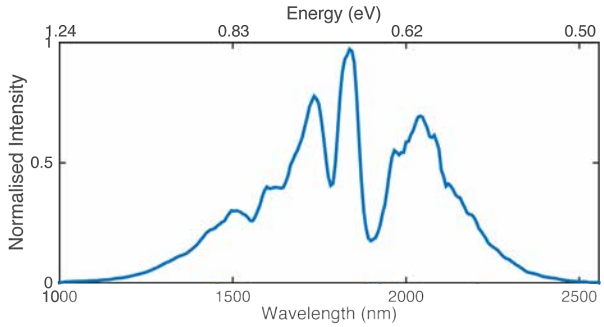

Fig. 1.1: Driving laser spectrum for HHG. The broadband spectrum output of the hollow-core fibre with a central wavelength of 1.85 μm is contained in a pulse with a duration of 12 fs.

1.1.3 CEP stability and control

When using few-cycle pulses as driving laser pulses for HHG, the spectral and temporal shape of the attosecond pulses is highly dependent on the CEP of its driving pulses[36,71–73]. Spectroscopic measurements require high spectral stability (with shot-to-shot fluctuations $< 1\%$) which means HHG must be generated from highly stable CEP pulses[72].

The idler output of the TOPAS is passively CEP-stable because it is generated via differential frequency generation (DFG) from a pump and signal (seed) pulse that originate from the same laser pulse. However, variations on the temporal synchronization between the seed and the pump will lead to CEP fluctuations on the idler. To compensate for long-term fluctuations in the CEP caused by for example environmental thermal fluctuations, we use an f-2f interferometer that extracts the relative CEP and feeds back to the second OPA stage in the TOPAS to compensate for temporal deviations in the synchronization[72]. Using this feedback loop to lock the CEP, the CEP fluctuations are measured with a standard deviation below 100 mrad rms over 72 hours.

The laser system used to produce the CEP-stable sub-2-cycle 1.85 μm driving laser pulses is in full detailed described in the reference S. L. Cousin et al.,[55] and in S. L. Cousin's Ph.D. thesis[74]. Section 1.2 shows how these pulses are sent to a beamline where they are focused into a high pressure gas target to produce isolated attosecond pulses in the soft X-ray regime[39–41,55].

1.2 XAFS beamline

Isolated attosecond pulses in the soft X-ray (SXR) regime, fully covering the water window, are generated via wavelength-scaled HHG using an ionisation phase-matching gating technique from CEP-stable sub-2-cycle 1.85 μm driving laser pulses.

To be able to use the described driving laser pulses for HHG, the pulses' electric field amplitude has to be comparable with the atomic potential of the medium used for HHG. Thus, intensities above 10^{14} W/cm^2 need to be reached to ensure tunnel ionisation and below 10^{15} W/cm^2 (1 PW/cm^2) to avoid full suppression of the coulomb potential. A peak intensity up to 0.5 PW/cm^2 is achieved by focusing the driving laser using a curved gold mirror with a focal length of 100 mm down to a 58 μm beam waist.

In addition, wavelength-scaling of the HHG process using driving lasers with central wavelengths at around 2 μm instead of the visible, leads to a tremendous decrease of efficiency scaled by the power of $\lambda_L^{-(5-9)}$ [32–35]. The decrease of photon yield in the single atom response can be microscopically compensated by coherently phase-matching the emitted radiation of individual atoms along the driving laser interaction with the HHG gas target. It has been demonstrated that this can only be achieved with high pressure gas targets to increase the weak plasma density in order to compensate for the delay of the driving laser propagation due to the neutral atoms[29]. The combination of a sub-2-cycle 1.85 μm driving pulse with a high pressure HHG target confines the phase-matching conditions to a temporal window within 50 as[40]. An upper limit of the pulse duration of 300 as can be placed by semi-classically estimating the attochirp of the generated spectrum[75].

To preserve a high photon flux, the generated radiation must travel in vacuum and thus avoid its absorption. The experimental arrangement of the beamline is shown in Fig. 1.2. The driving laser pulse is focused on a high pressure gas target to produce HHG radiation which co-propagates with the driving laser pulse. An aperture and a metallic filter are placed on the beam path to help reduce the pressure and block the driving laser beam, respectively. The soft X-ray radiation is refocused on a sample plane using a grazing-incidence ellipsoid mirror. The spectral components of the attosecond pulses are detected on a lab-built spectrograph using a grating and a charge-coupled device (CCD) camera.

In Sec. 1.2.1 the details of how a high pressure gas target can be achieved while maintaining a very low ambient pressure at the generation chamber are shown. Section 1.2.2 describes the propagation and re-conditioning of the generated radiation upon its detection to be able to use it for spectroscopic measurements.

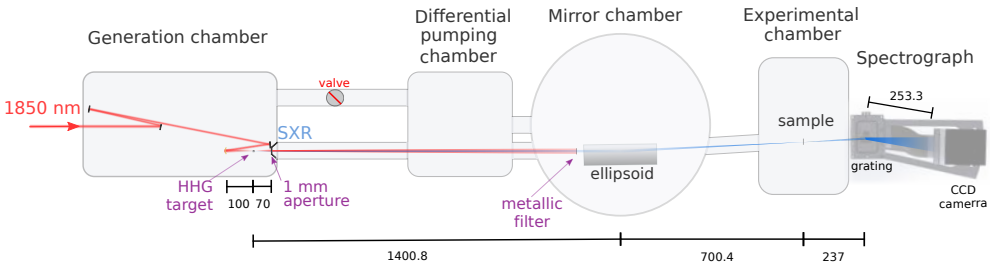

Fig. 1.2: HHG beamline. Attosecond SXR pulses are generated via the interaction of a high-intensity CEP-stable sub-2-cycle 1.85 μm laser and high-pressure gas inside a vacuum chamber (generation chamber). The SXR radiation co-propagates with the driving laser. A chamber for differential pumping is placed on the beamline to go from a few mbar to $1{\cdot}10^{-7}$ mbar of pressure using a 1 mm-diameter aperture. A metallic filter is placed in the beam path to block the remaining fundamental laser radiation. In the mirror chamber an ellipsoid focuses the SXR radiation into the sample plane in a 2:1 geometry. The radiation is spectrally resolved in a spectrograph that images the sample plane onto a CCD camera. Dimensions are shown with units of mm.

1.2.1 HHG generation in a high-pressure gas target

The challenge is to ensure a high gas pressure for the interaction with the high-intensity driving laser to generate attosecond pulses whilst keeping a low gas flow to minimize the ambient pressure around the target. Due to the high absorption of the soft X-ray radiation with soft matter (i.e. carbon based components) the radiation must be propagated in a vacuum. Figure 1.3 shows the HHG target design which consists of a 1.5 mm outer diameter (OD) tube with 0.5 mm inner diameter (ID) that has 2 holes concentric with the laser propagation and 0.3 mm in diameter. The gas can only stream out from the gas target through those 0.3 mm diameter holes. As a result of this design, a high-pressure zone is achieved in the interaction region.

The HHG target is connected with a 3 mm ID and 1 m long tube to a pressure gauge that measures the backing pressure. The pressure distribution at the interaction region along the HHG target is estimated by simulations performed using commercial computational fluid dynamics software. In the simulations the boundary conditions are set to match the experimental conditions while using a stationary laminar flow for the gas. Different gas elements, helium, nitrogen or hydrogen, have different viscosities and molecular sizes which lead to different particle flows while maintaining the same pressure distribution inside the gas target. Figure 1.4 shows the simulated pressure on axis of the HHG target.

The pressure distribution along the axis of propagation can be extrapolated

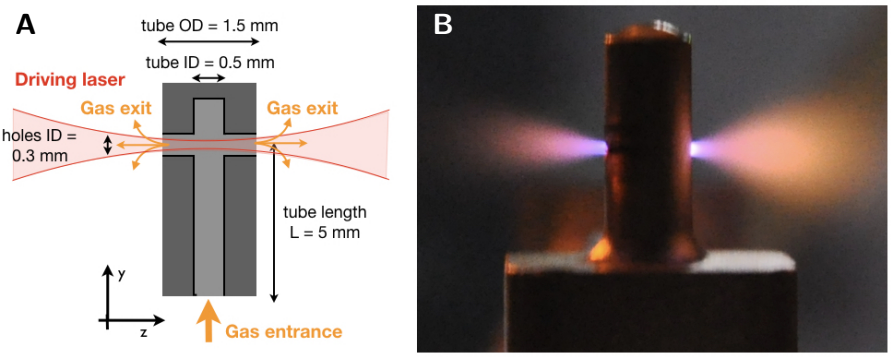

Fig. 1.3: High-pressure-gas HHG target. (**A**) Sketch of a vertical inner cut of the HHG target showing the entrance and exit of the gas together with the tubing dimensions and the driving laser interaction region. (**B**) Photograph of the HHG target during the generating radiation up to 160 eV in argon gas.

to other backing pressures by a numerical fit given by the analytical equation:

$$P = \frac{1}{4} P_{backing} \left(\frac{3}{1 + \left(\frac{2(|z| - 0.025)}{L} \right)^3} + \exp\left(-4 \cdot \ln(2) \left(\frac{z \pm 0.6384}{0.4} \right)^2 \right) \right), \tag{1.3}$$

where $P_{backing}$ is the measured backing pressure in bar, L = 0.75 mm is half the total target length and z is the geometrical coordinate in the laser propagation direction in mm with 0 at the target centre.

The simulations show that a measured backing pressure of 6 bar at the pressure gauge location relates to a maximum pressure on the target in the interaction region of 4.7 bar. The drop in pressure is highly dependent on the hole sizes from where the laser enters and exits the target and the tube ID. Increasing the tube ID by 100 μm leads to an increase of 1 bar of the maximum pressure in the target whilst an increase of the hole sizes of 80 μm in diameter leads to a pressure decrease of more than 1 bar. A smaller effect on the pressure distribution is given by the tube length from which an increase of 5 mm in length leads to a decrease a 0.5 bar (not shown). The hole sizes are kept as small as possible while not clipping the driving laser energy. The HHG target is made out of stainless steel to limit erosion caused by the high intensity laser increasing the hole size. The ID of the tube is kept as wide as possible while maintaining a robust structure that can be manufactured and ensuring that the overall thickness of the HHG target does not exceed 1.5 mm. A thin target is important because when using a curved focusing mirror for the driving laser the incident angle must be as close to 0 deg. as possible while crossing very close to the target. This small angle of incidence upon the focusing mirror is illustrated in Fig. 1.2.

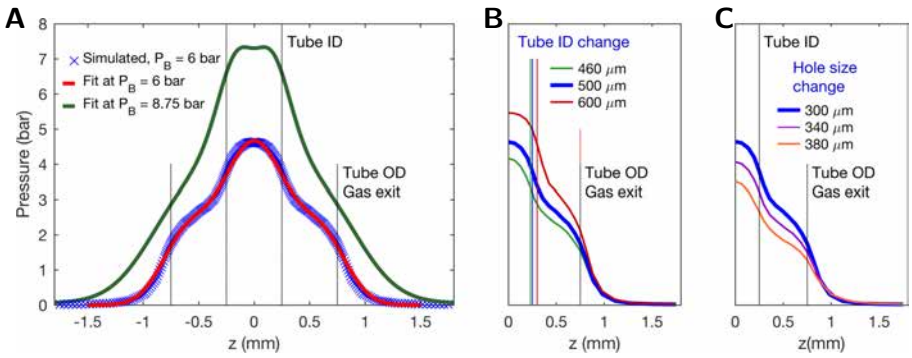

Fig. 1.4: Pressure distribution along the HHG target axis. (**A**) Simulated pressure distribution by computational fluid dynamics (blue crosses) at a backing pressure (P_B) of 6 bar and 20 mbar ambient pressure for the target geometry shown in Fig. 1.3. An analytical curve (Eq.(1.3)) is fitted (red solid curve) and extrapolated to a 8.75 bar backing pressure (green solid curve). (**B**) Simulated pressure distribution for different tube diameters. (**C**) Simulated pressure distribution for different hole sizes.

The simulated pressure distribution has been experimentally corroborated by interferometry. A phase shift is measured which is introduced by the total pressure of the target on the direction of the laser propagation. The phase shift is also measured transversally at the output of the target. A Mach-Zehnder interferometer is built at atmospheric pressure mimicking the scenario of the HHG target in vacuum. One arm of the interferometer has two focusing lenses with 100 mm focal length to focus a collimating Helium-Neon laser on the HHG target and re-collimate it to interfere with the other arm. The fringes are set vertically from which only a transverse line is recorded with a camera in order to achieve a high recording frame-rate. Firstly, the HHG target is set at the desired backing pressure. Then, the recording starts just before is slowly decreased ($\approx$ 1 bar/10 second) until it reaches an atmospheric pressure. Since the gas dynamics are governed by a pressure difference between two points, having the setup at atmospheric pressure instead of in vacuum only requires an increase the backing pressure of 1 atmosphere to match with the simulations. The expected number of shifted lines N is calculated by:

$$N = \sum_i \frac{x_i - x_{i+1}}{\lambda}(n(\tilde{P} - 1)), \tag{1.4}$$

where x defines a spatial coordinate (longitudinal or transversal) and x_i references to a specific sliced position, $\tilde{P}$ is the pressure between consecutive positions ($\tilde{P} = (P_i + P_{i+1})/2$), $\lambda = 632.8$ nm is the laser wavelength used and n is the refractive index of the gas which depends on the pressure. The experimentally measured line shifts in both directions, along and transversally to the HHG target, have a relative error of 12 % and 30%, respectively.

To minimize the ambient pressure around the HHG target, the vacuum chamber where the HHG target is placed is connected to a high capacity booster pump (Edwards EH250) and an oil-sealed rotary pump (Edwards E2M80) with a maximum displacement of 96 m^3/h and an ultimate vacuum of 10^{-4} mbar.

The combination of the target geometry together with the high capacity pump makes the ambient pressure stay at 11 mbar when using a backing pressure of 8.25 bar. Increasing the backing pressure up to 10 bar leads to an ambient pressure of 56 mbar. The system can hold backing pressures up to 20 bar while maintaining the ambient pressure below 100 mbar.

1.2.2 Beamline - SXR propagation and detection

The generated SXR radiation via HHG co-propagates with the driving laser field with a divergence inversely proportional to the harmonic order. During the HHG process different electron trajectories can recombine and release coherent radiation that will be generated at different times. These trajectories can be identified as long or short trajectories depending on their arrival times either at the full or half period of the driving laser field, respectively. Long trajectories lead to emitted radiation with a larger divergence[65,76] and due to their expected lower phase-matching capacity[68] they have never been measured using long-wavelength driving laser pulses. Still, to prevent them from interfering with short phase-matched trajectories a 1 mm aperture is placed 7 cm after the HHG target. This aperture is also used to facilitate increasing the pressure difference between the generation chamber and the consecutive chamber used for differential pumping, see Fig. 1.2.

1.2 m from the SXR radiation generation source an aluminium foil with a thickness of 100 nm is placed to block the co-propagating highly diverging 1.85 μm driving laser which is already partially blocked by the aperture after the HHG target. The diverging SXR radiation is refocused using a platinum-coated ellipsoidal mirror (Carl Zeiss Laser Optics) with $<$0.5 nm rms roughness at a grazing angle of incidence of 2 deg. to minimize losses. The ellipsoid is designed to image an object at 1400.8 mm on an image plane at 700.4 mm to achieve a 2 times demagnification. The HHG target is positioned at the object plane whereas the samples under study are positioned in the image plane. Pressure in the mirror chamber which contains the ellipsoid remains at 10^{-7} mbar whereas the experimental chamber, where the sample is placed, is at a pressure of 10^{-8} mbar.

The refocused radiation is analysed with a lab-built spectrograph consisting of a flat-field aberration-corrected reflecting concave grating (2400 lines/mm; Hitachi High Technologies America, Inc.) and a cooled (down to -70°C) CCD camera

(PIXIS-XO; Princeton Instruments). The grating is set to image the focal plane of the ellipsoid to the CCD camera in the dispersion plane (horizontal, x-z). A SXR spectrum is acquired between 250 eV and 1200 eV with a spectral resolution of 0.25 eV at 300 eV. The beamline details are fully described in the Ref. S. M. Teichmann et al., 2016[40], and in S. M. Teichmann's Ph.D. thesis[77].

Figure 1.5 shows the detected SXR radiation generated in helium on the spectrograph together with the spectral shape with a bandwidth of 195 eV and its divergence of 0.1 deg. from an extended beam size of 1.3 mm at FWHM. The divergence is calculated by considering a distance between the focal plane and the CCD camera of 472.3 mm which is the nominal distance provided by the grating's manufacturer.

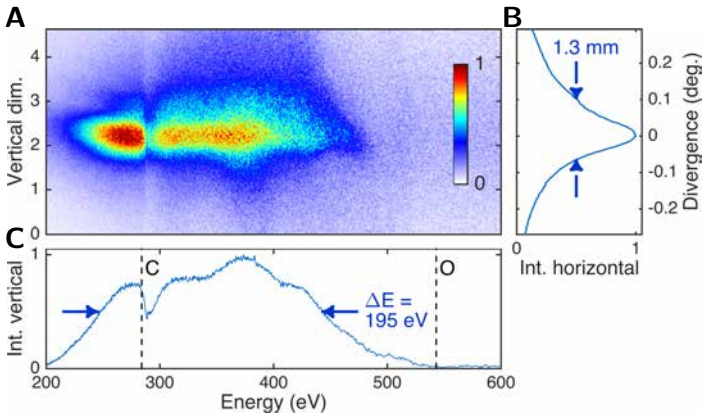

Fig. 1.5: Detected SXR radiation generated in helium. (**A**) shows the SXR counts on the spectrograph camera on a linear scale. (**B**) A SXR divergence of 0.1 deg. is obtained by horizontally integrating the counts in (A) with a beam size of 1.3 mm at FWHM. (**C**) A SXR spectrum is obtained by vertically integrated the counts in (A). The attosecond pulses contain a 195 eV spectral bandwidth fully covering the water window from the carbon K-shell edge at 284 eV to the oxygen K-shell edge at 543 eV. Clearly visible is residual carbon absorption at the K-shell edge.

The generated radiation is highly dependent on the driving laser peak intensity, CEP value, beam profile, position with respect to the focal plane and gas pressure. The spectral dependence on these terms is detailed in Chap. 2. Flux and cutoff energy of the generated radiation are optimised by iteratively adjusting all of these parameters on which the radiation is dependent. Firstly, the driving laser is focused and sent through the HHG target holes. This alignment starts with a co-propagating helium-neon laser (at 632.8 nm) that as well as being visible it also does not damage the HHG target. If the high intensity 1.85 μm pulses touch the walls of the target's holes, they will abate the material' thus modifying the HHG target which is designed to minimise the gas flow. After aligning, the gas

pressure is raised to a pressure that maximises the signal. The typical indicated backing pressure values are around 0.9 bar for argon, 3.5 bar for neon and 8.5 bar for helium, which leads to cutoff energies of 160 eV, 400 eV and 550 eV, respectively. A signature that the HHG target's input hole for the laser is damaged, such that its area has increased due to ablation, is that the maximum HHG yield is achieved using backing pressures higher than the nominal pressure values, i.e., to obtain the same ideal pressure in the interaction region the backing pressure must be increased. If this is the case the target needs to be replaced. Subsequently, the aperture of an iris which is placed just before the beamline entrance at around 2 meters before the HHG target is adjusted to further optimise the signal. The aperture modifies both the intensity at the interaction region and its beam profile [78–80]. Finally, the target position and consequently the laser beam propagation direction are fine tuned. Iteratively the gas pressure, the iris aperture, target position and the beam propagation direction are adjusted to increase the signal strength until the maximum HHG yield is achieved. Figure 1.6 shows detected spectra directly integrated on the CCD in two cases, when the CEP is shuffled and when it is locked. The integration time is set to 1 minute for each spectrum. These spectra are taken with an extra 100 nm aluminium filter placed at around 8.5 cm before the camera.

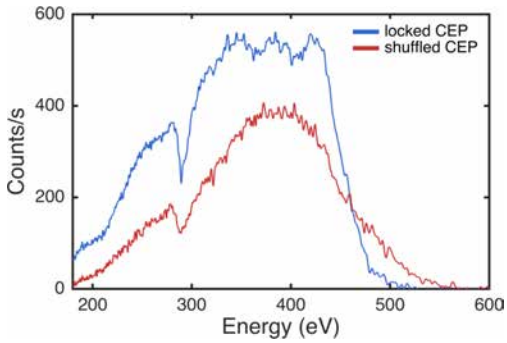

Fig. 1.6: Spectral CEP dependence of the attosecond SXR pulse. The spectra are integrated over 1 minute. When the CEP is locked, its rms deviation is lower than 100 mrad.

The detected photon counts ($S_{detected}$) are one order of magnitude smaller than the estimated number of photons at the sample plane ($S_{SamplePlane}$). The drop in photon count is caused by the low refractive efficiency of the existing gratings. Figure 1.7 shows the spectrograph response due to the CCD camera (R_{CCD}), the grating refraction ($R_{grating}$) and the transmission of an aluminium 100 nm filter ($R_{Al100nm}$) together with the estimated photon spectra incident upon the sample which is calculated by:

$$S_{SamplePlane} = \frac{S_{detected}}{R_{CCD} \cdot R_{grating} \cdot R_{Al100nm}}. \tag{1.5}$$

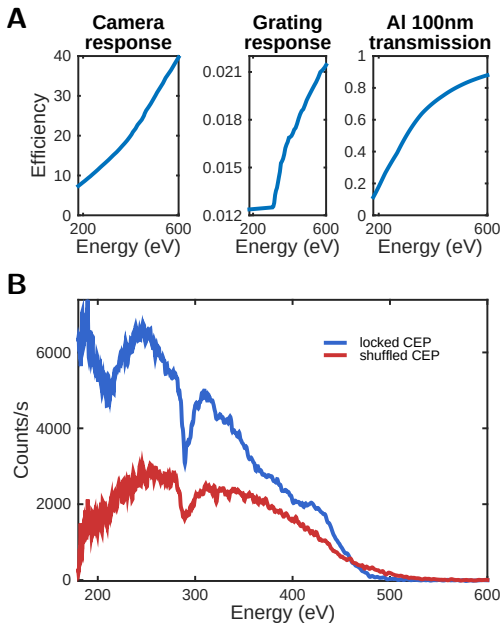

Fig. 1.7: Spectral detection response. (**A**) shows the spectrograph response from the CCD camera, the grating refraction and the transmission through an aluminium filter with a thickness of 100 nm. (**B**) Estimated spectra at the sample plane calculated from the detected spectra shown in figure 1.6.

The SXR beam size at the focal plane, shown in Fig. 1.8, is measured using the knife edge method by scanning a pinhole with 50 μm inner diameter in steps of 10 μm over an area of 300 μm x 300 μm. The integrated spectral signal is acquired over 3 seconds at each pinhole position.

The measurement yields a SXR beam waist of 80 μm at the target plane for photon energies between 400 and 500 eV, whilst the average beam waist is 50 μm when taking into account the whole attosecond spectra. The SXR beam size at the sample plane is also shown as a function of the detected spectral energy of the beam. The beam size increases when averaging higher photon energy ranges. Intuitively one could think that since lower photon energies are easier to generate due to needing a lower driving laser peak intensity, they would be produced over a larger area. What is demonstrated here is that larger beam sizes correspond to higher photon energies closer to the cutoff energy.

The SXR radiation, which fully covers the water window with photon energies from 200 eV to 550 eV, at the sample plane has a total number of photons of $6.5{\cdot}10^3$ which leads to a pulse energy of 0.2 pJ that is focused down to a 50 μm beam waist yielding a fluence of 7 nJ/cm^2. This radiation, confined in an isolated attosecond pulse with duration below 300 as can be used for spectroscopic measurements

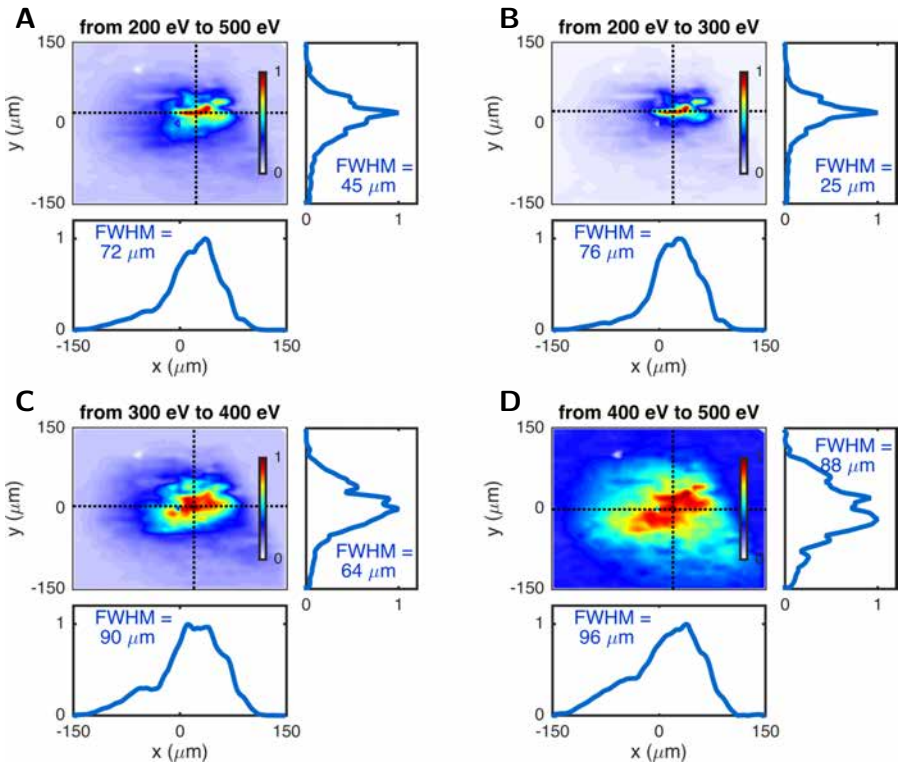

Fig. 1.8: Spectrally resolved SXR beam size at the sample plane. (**A-D**) The result of a knife edge measurement of the SXR beam spectrally integrated across the specified energy ranges is shown. A 50 μm pinhole is scanned in 10 μm steps while integrating the signal over 3 seconds at each step position. We measure the beam size at FWHM (horizontal x vertical): (**A**) 45 μm x 72 μm with the full SXR spectrum; (**B**) 25 μm x 76 μm from 200 eV to 300 eV; (**C**) 64 μm x 90 μm from 300 eV to 400 eV; and (**D**) 88 μm x 96 μm from 400 eV to 500 eV. An increase of beam size can be seen as the energy of the spectral range increases.

such as X-ray absorption spectroscopy fine structure (XAFS)[55]. Details on the fundaments of this technique and the application of it in the beamline are shown in Chap. 3.

1.3 Time-resolved XAFS setup

Field-driven electron dynamics can be probed with attosecond resolution using the generated attosecond SXR pulses when synchronising them with a femtosecond laser pulse on a given sample. This technique is generally categorised as the pump/probe scheme. The femtosecond pulse is used as a pump to initiate electron dynamics that are probed in time by the attosecond pulse by changing the delay

between these two pulses. Zero time delay is assigned to the temporal overlap of the maximum electric field of both pulses. Positive delays are assigned to the pump pulse arriving first to the sample thus the initiated dynamics can be probed as a response of the pump. Negative delays instead, are associated with the probe pulses arriving first, followed in time by the pump pulses. Since light travels 3 nm in 10 as, the synchronisation between the pump and probe pulses must happen within a few nanometers to ensure attosecond resolution. A minimised temporal jitter is achieved by having both pump and probe pulses born from the same source.

Depending on the sample properties under study and the electron dynamic processes that one would like to probe, different pump pulses must be used. For small bandgap semiconductors or semimetals pump pulses with longer central wavelengths (with small photon energies) will easily excite electrons from the valence to the conduction band through a single photon absorption. Whereas insulators or wide-bandgap materials need higher photon energies for a single photon absorption. When probing field-driven electron dynamics CEP-stable pump pulses are needed to have temporal shot-to-shot field reproducibility. However, dynamics happening within a few tens of femtoseconds like for example molecular vibrations or lattice dynamics do not require pump pulses with CEP stability. Moreover, the control over the pump intensity and beam polarisation allow us to choose the physical mechanism involved in the initiated dynamics.

Here, 3 different setups for generating pump pulses are presented. Two of them have pump pulses that are generated from a replica of the driving laser pulses used for HHG, at central wavelengths of 1.85 μm and 800 nm, which are described in Secs. 1.3.1 and 1.3.2, respectively. These pumps are CEP-stable allowing electric field driven dynamics to be probed. In Sec. 1.3.3, a third setup shows the possibility of having a high fluence control over the pump with a 800 nm pulses coming directly from the left over pump pulse of the 3rd OPA stage in the TOPAS.

1.3.1 1.85 μm CEP-stable pump

Probing field-driven dynamics in small bandgap semiconductors or semimetals initiated by single photon absorption requires CEP-stable pump pulses with low photon-energy spectral components. An in-vacuum Mach Zehnder interferometer is built to synchronise a sub-2-cycle CEP-stable 1.85 μm (0.67 eV) pump pulse with the generated isolated attosecond pulses (in the SXR) in order to probe the induced dynamics via XAFS. A diagram of the setup is shown in Fig. 1.9. A beam splitter (Thorlabs BP108) reflects 3% of the total incident pulse energy and sends it to the pump beam path. A 0.39 mJ beam that is transmitted through the pelli-

cle is focused into a helium gas target in order to generate attosecond pulses via HHG. The beam reflected from the pellicle is sent to a delay stage with sub-nm resolution (SmarAct SLC-1730) and minimum step width of between 1 and 1.5 nm. In the differential pumping chamber a fused silica window with a thickness of 400 μm is placed at the Brewster angle to block gas flow from the generation chamber to the mirror chamber due to the new beam path for the pump. This thin Brewster-window does not increase the pump pulse duration by more than 2 fs.

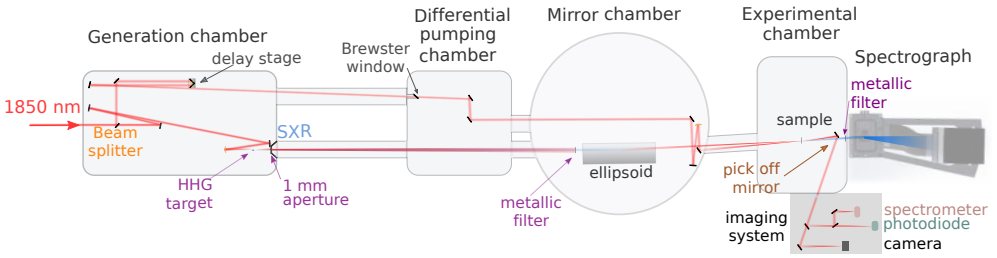

Fig. 1.9: CEP-stable sub-2-cycle 1.85 μm pump - attosecond SXR probe experimental setup. A beam splitter, which placed inside the generation chamber before the HHG target, reflects 3% of the CEP-stable sub-2-cycle 1.85 μm pulses and sends them to the pump beam path with a nm precision using a delay stage that controls the synchronisation between the pump and the SXR probe pulses. The directed pump through the beamline is focused on the sample plane using a mirror with a 500 mm focal length that sits on the mirror chamber. A pick off mirror in the experimental chamber sends the transmitted pump through the sample to an imaging system outside the beamline. In the imaging system the pump beam size at the sample plane is measured whilst the pump intensity and the pump spectrum are also recorded during the time-resolved XAFS measurements as a function of the pump-probe time delays.

In the mirror chamber the pump beam is conditioned to be focused on the sample plane using a mirror at normal incidence with a small angle with a focal length of 500 mm. A 45 deg. mirror steers the beam onto the sample plane in a non-collinear configuration with respect to the soft-X-ray beam, which has an incidence angle of (3.7 $\pm$ 0.3) deg. smaller than the SXR beam angle. Due to various gold and silver mirror reflections in the sample plane the pump pulses have a power of (4.8 $\pm$ 0.5) mW with a beam size of (300 $\pm$ 30) μm x (200 $\pm$ 20) μm at the FWHM, at the horizontal and vertical axis, respectively. This leads to a pump incidence fluence of (10 $\pm$ 2) mJ/cm^2. The pump polarisation is preserved as the p-polarised defined as contained in the plane of incidence.

The slight non-collinearity allows the pump beam to be picked off with a mirror downstream of the sample plane which steers the transmitted pump beam out of the experimental chamber through a viewport to an imaging system. In the imaging system both the pump's intensity stability and spectral components are

recorded. For the pump-probe experiments an additional aluminium filter with a thickness of 100 nm is placed in front of the SXR camera to block any scattered or stray light from the pump beam. A hard aperture is paced on top of the sample to ensure spatial overlap of the IR pump and SXR probe beams, thereby preventing any possible mismatch between the excited and probed volume inside the target. The aperture consists of a 20 μm-thick nickel disc of 3 mm outer diameter and a 100 μm inner-diameter hole. The outer diameter of the disc is much larger than any of the beams which ensures that only the 100 μm hole transmits the pump and probe beams through the sample. The thickness of 20 μm is sufficiently large to block any transmission of the SXRs. The pinhole furthermore, defines the entrance slit to the spectrograph as it is placed together with the target sample in the entrance-slit plane of the flat-field spectrograph.

1.3.2 800 nm CEP-stable pump

Higher photon energies for the pump pulses are needed when exciting direct electron transitions between valence and conduction band in wide-bandgap semiconductors through single photon absorption. In metals or semimetals, these pump pulses can be used to initiate electron transitions resulting in a higher energy difference between the created hole density and excited electron density seen on the X-ray absorption spectrum. Figure 1.10 is a diagram of the attosecond time-resolved XAFS experimental setup pumped with CEP-stable 800 nm pulses. CEP stability is used to preserve the ability of probing field-driven electron dynamics. A pellicle beamsplitter with a reflectivity of 13% (Thorlabs BP14B3) at 1.85 μm is used to reflect 40 mW of the sub-2-cycle CEP-stable 1.85 μm pulses which are used for generating the attosecond SXR radiation. The reflected energy is sent to the synchronised delay line used for the pump beam path. After travelling through the Brewster-window that separates the generation chamber from the differential pumping chamber, the 1.85 μm beam is focused with a mirror at normal incidence with a small angle with a focal length of 500 mm down to a 1 mm beam waist to achieve an intensity of 65 GW/cm^2. A 0.6 mm thick BiBO crystal (Newlight PO:20090210, Φ: 11.3 deg.) is placed close to the focal plane such that second harmonic generation (SHG) of the 1.85 μm beam occurs. An additional 500 mm focusing mirror is placed in the mirror chamber to collimate the SHG beam that co-propagates with the non frequency converted 1.85 μm beam. These co-propagating beams are reflected on two dichroic mirrors (Layertec 103472) with high reflectivity of 99% at 800 nm at 45 deg. and low p-polarised reflectivity (less than 3% at 45 deg.) across a bandwidth from 1200 nm to 2800 nm.

A focusing mirror with a small angle of incidence with a focal length of 500

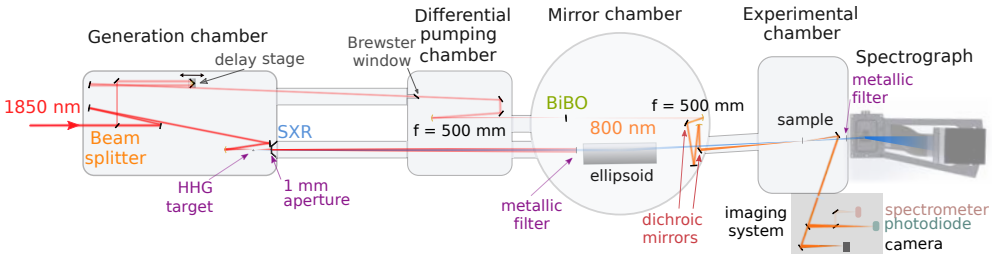

Fig. 1.10: CEP-stable 800 nm pump - attosecond SXR probe experimental setup. Further to the setup shown in Fig. 1.9 a beam splitter is replaced from 3% reflectivity to reflect 13% of the CEP-stable sub-2-cycle 1.85 μm pulses and send them to the synchronised delay line. The reflected 1.85 μm beam is focused on a BiBO crystal with a f = 500 mm mirror placed in the differential pumping chamber to cause SHG which is polarised perpendicularly to the 1.85 μm beam. In the mirror chamber the beam is collimated with another f = 500 mm mirror. Two dichroic mirrors are used at 45 deg. to reflect 99% of SHG signal and only 3% of the left over 1.85 μm beam. The SHG pump is focused on the sample plane with a mirror with 500 mm focal length. A pick off mirror sends the transmitted pump beam through the sample to an imaging system outside the beamline where the pump beam size at the sample plane is measured. The pump intensity and the pump spectrum are also recorded during the time-resolved XAFS measurements as a function of the pump-probe delay.

mm focuses the SHG beam on the sample plane down to (160 $\pm$ 10) μm x (140 $\pm$ 10) μm at the FWHM, at the horizontal and vertical axis, with an energy of (3.6 $\pm$ 0.5) mJ from which 1% is estimated to belong to the remaining 1.85 μm. Figure 1.11 shows the spectrum and beam size of the SHG beam. The spectrum with a bandwidth that has a Fourier limit of 10 fs is detected in the imaging system after being reflected on both dichroic mirrors. The beam size is measured directly on the sample plane by scanning a 50 μm ID pinhole over a 400 μm x 400 μm area with 10 μm steps and recording its transmission with a photodiode which is also placed in the imaging system. The photodiode signal is integrated over 100 ms at each pinhole position.

The 800 nm CEP-stable pump has an s-polarised fluence of (21 $\pm$ 3) mJ/cm^2 at the target plane. Although the same approach of sending the pump beam out of the experimental chamber with a pick off mirror and using an extra metallic filter in front of the X-ray CCD camera are implemented, the X-ray camera sees a larger photon count coming from stray light of the pump beam rather than counts generated by the attosecond SXR spectrum. To minimise the detection of the stray light from the pump beam one could place apertures along the SXR propagation. This procedure must be implemented before performing measurements with pump photon energies above the silicon bandgap (1.1 eV). The X-ray CCD chip detector

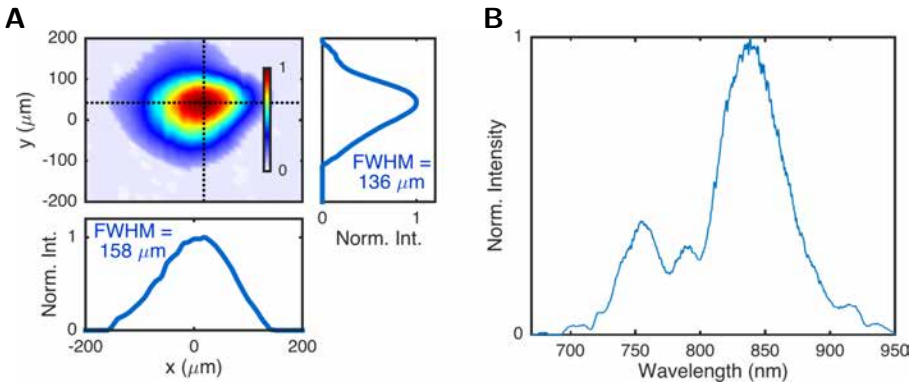

Fig. 1.11: CEP-stable 800 nm pump beam size and spectrum. (**A**) A 800 nm wavelength beam size measured as 160 μm x 140 μm at the FWHM at the sample plane with a knife edge technique. A photodiode integrates the transmitted photon signal through a 50 μm ID pinhole scanned across the 400 μm x 400 μm area with 10 μm steps and 100 ms integration time. (**B**) Broadband 10 fs Fourier limited spectral intensity of the SHG of the 1.85 μm beam measured at the sample plane with 10 ms integration time.

is made of silicon and its detection efficiency is lower for photon energies below the bandgap.

1.3.3 800 nm pump with fine-tuned fluence

The previously shown pump-probe setups, in Figs. 1.9 and 1.10 in the above sections, where the Mach-Zehnder interferometer starts inside the beamline, are limited in tunability of the fluences. To modify the fluence of the pump to an optimum, the fluence can be decreased by introducing pellicles along the pump beam path that reflect part of the pulse energy. These pellicles can be as thin 30 nm and are made out of silicon nitride (Silson, Si_3N_4 windows) which reflects only a few percent of the total pulse energy. Thus, to significantly reduce the pump fluence many thin films are needed which increases the beam path through the material and eventually leads to a walk-off (deviation) of the original beam path. Otherwise, the pump fluence can be made larger by increasing the reflectivity of the pellicle which is used for splitting the 1.85 μm pulse energy into the transmitted driving pulses for HHG and the reflective pump pulses. The increase of the energy used for the pump is at the expense of the energy used for the HHG process thus limiting the cutoff photon energy according to Eq.(1.1).

Here an alternative approach to tune the fluence of a 800 nm beam is presented where the fluence can be changed from the maximum value to the minimum

without suffering from changes in beam path by using a half-waveplate and two polarisers. The TOPAS output spatially separates the left over 800 nm pulses used to pump the 3rd OPA in a slightly non-collinear configuration. These pulses have a poor-quality beam profile contain 2.8 mJ of energy and have a pulse duration of around 80 fs. To compress them down to few-femtoseconds 1.05 mJ of their energy are sent into a hollow-core fibre (HCF) with ID of 0.3 mm that is filled with 1.1 bar of argon which cleans the beam profile and broadens their spectrum to a 5 fs Fourier limit, see Fig. 1.12. The output of the HCF with an energy of 0.26 mJ is collimated and sent to a pair of chirped mirrors (Layertech 103624, GVD (510-930 nm) = (-40 $\pm$ 20) fs^2) that compensate for the pulse chirp and material dispersion along the pump beam path to compress the pulses down to 15 fs using 6 bounces.

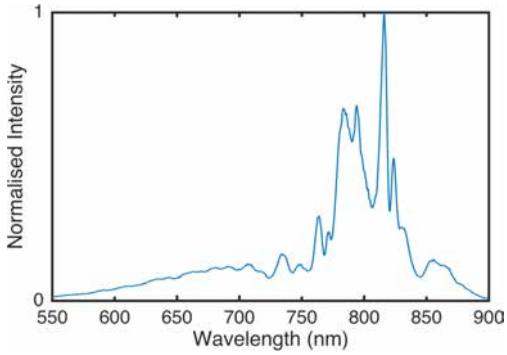

Fig. 1.12: 800 nm fluence-controlled pump spectrum. Intensity of the left over 800 nm beam from the TOPAS with a spectrum broadened with a hollow-core fibre that has a 300 μm ID filled with 1.1 bar of argon. The spectrum has a 5 fs Fourier limit bandwidth.

The fluence is controlled by sending the pulses through a half-waveplate (B-halle achromatic from 500-900 nm) mounted on a rotatable mount with 565 steps within 90 deg. of rotation (0.16 deg./steps). The half waveplate rotates the linear polarization of the pulses. Afterwards 2 fused silica wedges have their front surfaces placed at the Brewster angle in order to reflect only s-polarised radiation. One could use this polarisation directly, but instead the beam is sent to a 90 deg. periscope to change the pulses to p-polarisation and send them into the beam line with a small angle with respect to the 1.85 μm pulses, see Fig. 1.13.

The beam size at the sample plane is highly non-symmetric characterised by the imaging system to be (640 $\pm$ 60) μm x (164 $\pm$ 16) μm at the FWHM for the horizontal and vertical axes, respectively. After the reflections from both wedges the power of the beam can be tuned from (7.0 $\pm$ 0.5) mW to less than 0.5 mW. By changing the power we are able to tune the fluence as a function of the waveplate rotation as shown in Fig. 1.14. This power value (7.0 $\pm$ 0.5) mW leads to a

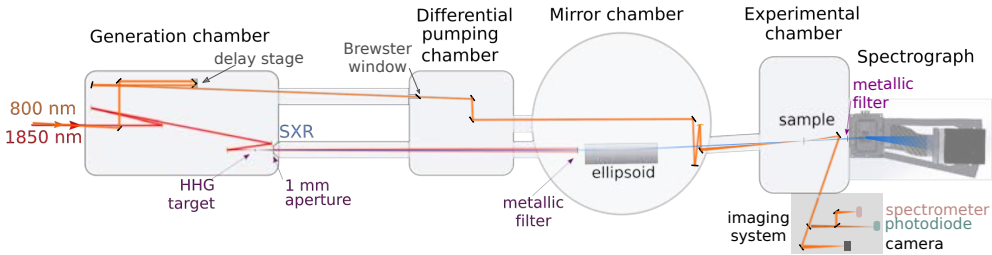

Fig. 1.13: 800 nm fluence-controlled pump - attosecond SXR probe experimental setup. The 1.85 μm driving laser and pump beams share the input beamline mirror with a slightly different angle. The pump with a 15 fs pulse duration and a central wavelength of 800 nm comes from the compression of the left over pump beam of the last OPA in the TOPAS. All the 1.85 μm pulse energy is used for HHG and the 800 nm pump beam is steered to the delay line without interfering with driving laser beam or needing to modify any beam path from the setup shown in Fig. 1.9 . The added beam path due to the pump beam compression is adjusted with respect to the 1.85 μm beam path before the beamline entrance.

maximum fluence at the sample plane of (2.0 ± 0.6) mJ/cm^2.

The advantage of this set up, apart from being able to accurately control the pump fluence at the target plane without modifying the spatial-temporal pump-probe overlap, is that the full 1.85 μm pulse energy can be used for the HHG process if needed such that the cutoff energy is extended to its maximum photon energy. In addition, the pulse duration can be minimised and measured outside of the beamline. However, a drawback is that the pulses are not CEP stable, thus field-driven electron dynamics cannot be seen although dynamics that occur within a few tens of femtosecond can already be resolved. The pulses could be compressed down further to sub-2-cycles, if their spectra were more broadened on the HCF[81]. As for making those pulses CEP stable, one could try to generate a broadband spectrum that covers the range from 400 nm to 900 nm and non-linearly compose them via differential frequency generation (DFG) such that the random CEP is cancelled. However, if the frequency intensity at those wavelengths is already poor (although after having optimised the DFG process) the output signal might still be too weak to be used which is the current scenario.

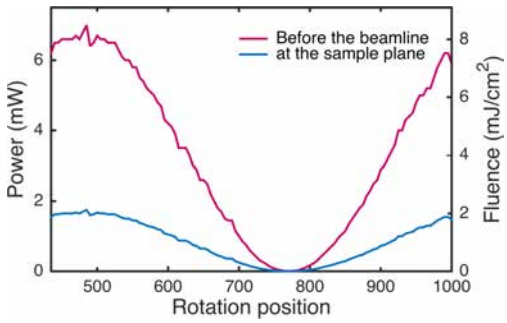

Fig. 1.14: 800 nm pump fluence-controlled using a half-waveplate rotator. Showing the pump power before the beamline and at the sample plane varies as a function of a half-waveplate rotation (with 565 steps) from position 435 to 1000 covering a rotation of 90 deg. The fluence indicated on the right vertical axis only refers to the beam at the sample pane. The half waveplate rotates the pump polarisation. The s-polarised part of the pulses is reflected on the front surface of a pair of wedges at a Brewster angle. The polarisation is flipped back to p-polarisation using a 9 deg. periscope.

1.3.4 The pump-probe's temporal overlap

The temporal overlap between the pump and the SXR probe pulses only occurs during approximately the pulse duration of the pump, 12 fs at FWHM. To measure the induced electron dynamics of the pump on a material, it is important to scan time delays over tens of fs with attosecond resolution. This time delay scan corresponds to changes of optical beam path over at least 5 μm with steps of 60 nm (200 as). Hence, the optical beam paths that these pulses travel (of $\approx$ 2.5 m) must be matched within 5 μm in order to be able to overlap the pulses in time. Such a high accuracy (of microns) of measuring the optical beam path over meters cannot be achieved using conventional rulers. Here, in this section it is explained how the temporal overlap between these pulses can be confined as much as possible in order to decrease the range of the time delay scans for the measurements.

Firstly, this temporal confinement between the pump pulses and the driving laser pulses for the HHG is found within $\pm$ 30 ps which is equivalent to a $\pm$ 9 mm path length. Both the HHG target and the metallic filter upstream of the ellipsoid mirror are removed from the 1.85 μm - SXR beam path. For this measurement, both pump and driving laser beams are sent to the imaging system using the pick off mirror. The high rising edge (500 ps) photodiodes (Menlo APD310 and APD210) are connected to a sampling (Lecroy, 40 GS/s with 1.5 GHz - 6 GHz bandwidth) oscilloscope. One of the photodiodes is set to detect only the pump beam which is used as a trigger. The second photodiode is positioned at the focal

plane of the imaging system which corresponds to the image plane of the sample plane. This photodiode detects both beams at the same time. The beam paths of both arms are adjusted until the rise edge of signals on the oscilloscope overlap in time.

To further confine the temporal overlap between the pulses, one can look for spectral and spatial interferences between pump and probe beams using the spectrometer and the CCD camera, respectively, in the imaging system. This can only be applied for pulses containing the same spectral components with the same polarisation. However, since the 1.85 μm pulses used for HHG have a large bandwidth down to the near-infrared, this technique can also be applied for pump beams with a central wavelength at 800 nm. In that case a bandpass filter at (800 $\pm$ 40) nm is placed in the 1.85 μm beam path to match with the pump spectrum. Spectral interferences are a bit more difficult to find than spatial fringes since they disappear at zero delay. However, spatial fringes intrinsically appear at the spatial-temporal overlap on the CCD camera due to the slight non-collinearity between the pump and probe beams, see Fig. 1.15. Another requirement is that both beams must have similar intensities to increase the visibility of the interferences. If attenuation filters have to be placed to achieve similar intensities this changes the optical path length meaning that no direct measurement of the zero delay is possible.

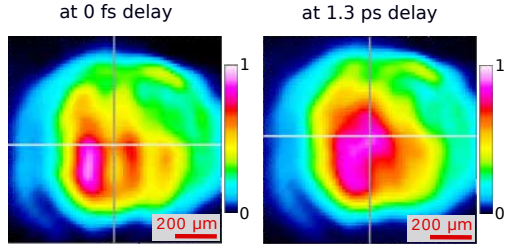

Fig. 1.15: Spatial interferences at the spatio-temporal pump-probe overlap. Vertical fringes appear on the CCD camera in the imaging system when 0 fs delay between a 800 nm pump and the 1.85 μm driving laser beams occurs. Both beams are p-polarised and have spectral components at around 800 nm. To increase the interference visibility firstly a bandpass filter centred at a wavelength of (800 $\pm$ 40) nm is placed in the 1.85 μm beam path and secondly the beam intensities of both beams are attenuated to have similar intensities.

A finer temporal confinement of the beam paths to within 30 fs of each other (which is equivalent to 30 μm beam path) is achieved by the sum frequency generation (SFG) between the the pump beam and the left over part of the 1.85 μm driving laser beam that is directly measured in the sample plane with a non-linear BBO crystal. Figure 1.16 shows the generated SFG signal as a function of the time delay between the driving laser pulses and three different pump pulses.

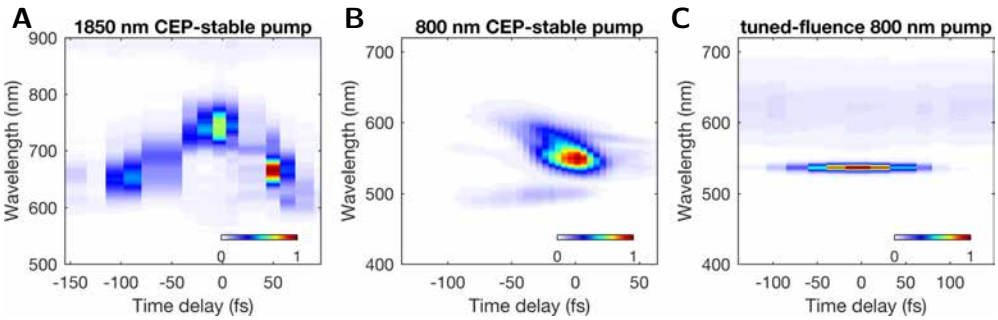

Fig. 1.16: Time-delay scan of the SFG of the indicated pump and the 1.85 μm driving pulses on a BBO crystal at the sample plane. (**A**) A (20 $\pm$ 10) μm BBO crystal that sits on a (1.0 $\pm$ 0.1) mm thick ultraviolet fused silica (UVFS) substrate with $\theta = 25.6$ deg. is used to combine the driving laser pulses with 1.85 μm CEP-stable pump pulses which are replicas of the driving laser pulses. Both beams are p-polarised. The signal at 750 nm is assigned to the SFG of 1.5 μm with 1.5 μm wavelengths from each beam. The signal at 660 nm can be seen to be coming from a SFG between 1.5 μm and the SHG of the 1.85 μm pump pulses which is delayed by 50 fs. (**B**) The SFG signal is generated using the same BBO as in (A) but combined with a 800 nm CEP-stable pump pulse that comes from the SHG of a replica of the 1.85 μm driving laser pulse. The pump beam is s-polarised which is perpendicular to the driving laser beam polarisation. The estimated efficiency of the SFG process only decreases by 16% when compared with the scenario in (A). (**C**) A 1 mm BBO crystal with $\theta = 23$ deg. is used to combine the driving laser with 800 nm pulses that are generated from the left over intensity of the TOPAS which are then compressed using a hollow-core fibre to broaden the spectrum and chirped mirrors to compensate for dispersion. These pump pulses have a finely controlled fluence and the same p-polarisation as the driving laser beam. The large temporal overlap between both beams indicated by a SFG with a FWHM signal of 70 fs is due to the large thickness of the BBO that introduces a group velocity phase mismatch of 40 fs/mm.

Figure 1.16A shows the SFG signal of the driving laser pulse with a 3% replica of its total energy, see Sec. 1.3.1. The SFG signal from both p-polarised beams is generated on a BBO crystal with a thickness of (20 $\pm$ 10) μm that sits on a (1 $\pm$ 0.1) mm thick UVFS substrate which is placed on the sample plane. The BBO crystal's orientations are $\theta = 25.6$ deg. and $\Phi = 90$ deg., where θ is the angle between the optical path and the optical axis and Φ is the angle between the tuning plane and the phase matching plane along the optical path. Φ should be assumed as 90 deg. unless it is specifically stated otherwise. The SFG signal as a function of the time delay is observed, the beams temporally overlapped at a delay 0 fs, a measurement is taken with a central wavelength of 750 nm which comes from the SFG between the spectral range around 1.5 μm of both pulses. The signal at 660 nm is assigned to the SFG between the 1.5 μm signal from the left-over part of the driving pulses and the second harmonic of the pump pulses

which is delayed by about 50 fs compared to the signal at 750 nm.

Figure 1.16B shows the SFG signal of the driving laser pulse with the SHG of a 13% repica of its total energy, see Sec. 1.3.2. The same BBO crystal as in figure 1.16A is used. However, the estimated efficiency drops by 16% with the combination of the p-polarised 1.85 μm and the s-polarised 800 nm beams.

Figure 1.16C shows the SFG signal of the driving laser pulse with the left over part of the pump beam of the TOPAS that is then compressed using a hollow-core fibre and chirped mirrors, see Sec. 1.3.3. In this case a BBO crystal with a thickness 1 mm and $\theta = 23$ deg. is used. The 1 mm length of the BBO crystal causes a group velocity phase mismatch of 40 fs due to the different wavelengths. This is the reason why the SFG signal has a large FWHM of 70 fs which is larger than the correlation of a 12 fs 1.85 μm pulse with a 15 fs 800 nm pulse.

1.4 Conclusion

Isolated attosecond pulses in the SXR are generated via ponderomotive scaling HHG and using phase-matching conditions for temporal gating[40,41]. A CEP-stable driving laser is focused on a high pressure helium target from where p-polarised SXR attosecond pulses are generated which have a duration below 300 as and a spectrum from 200 eV to 550 eV that can be tuned and covers the entire water window. The generation, propagation and spectral detection of the attosecond SXR pulses happen in an in-vacuum beamline. At the sample plane the SXR pulses are focused down to a 50 μm beam waist with a flux of $6.5{\cdot}10^3$ photons which leads to a pulse energy of 0.2 pJ and a fluence of 7 nJ/cm^2

A femtosecond infrared (IR) laser pulse is synchronised with the attosecond SXR pulse. The IR pulse is used to initiate (pump) electron dynamics in materials that will be probed by the attosecond pulses as a function of the time delay between both pulses. The pump pulse can be CEP-stable with a fluence of up to tens of mJ/cm^2 produced as a replica from the 1.85 μm driving laser pulse used for HHG. The SHG from this pump pulse can also be used as a pump pulse and potentially one could double the frequency again and obtain a 400 nm pump pulse. However, pump photon energies above the silicon bandgap at 1.1 eV can be detected by the X-ray CCD camera and so special care needs to be taken to avoid stray light being detected. The left over 800 nm beam from the TOPAS can also be used as a pump with finely tunable fluence and a careful compression setup is introduced before the beamline at the expense of not having CEP-stable pulses.

The spatio-temporal overlap between pump and probe pulses within 30 fs is

achieved by the SFG in a BBO crystal located at the sample plane. The left-over energy of the 1.85 μm driving laser pulse used for HHG is used as a probe which can reach the sample plane if the metallic filter is removed from the beam path.

2 Tailoring attosecond soft X-ray pulses

This chapter shows the capability of generating SXR isolated attosecond pulses in the water window with tunable spectra via manipulating macroscopically the HHG process by changing phase-matching terms such as plasma dispersion and Gouy phase.

Firstly, in Sec. 2.1 a brief introduction of phase matching terms that occur in the HHG process is presented. The influence on the generated radiation by changing macroscopically the HHG target pressure and the HHG target position with respect to the driving laser focal plane are shown in Secs. 2.2.1 and 2.2.2, respectively. The spectral changes dependence on phase matching terms is discussed and compared to the response caused by a change in the CEP value in Sec. 2.3. The effect of a plasma-induced defocusing is also discussed. The chapter ends with the conclusions in Sec. 2.4.

2.1 Introduction to phase matching terms

During the HHG process, phase matching between the driving laser and the HHG generated radiation phases has been demonstrated to be a crucial parameter to ensure the build-up of the coherently emitted radiation[29,45] and also ensure that the radiation is emitted in a single attosecond pulse[40,68,82]. What has not been yet explored is how the whole generated spectrum changes depend on phase matching conditions when ponderomotive scaling the HHG process and how one can use them to tune the generated spectrum according to the applications for which the system is to be used.

Microscopic phase matching consists of minimizing the phase mismatch between the driving laser pulse and the generated radiation such that $\Delta\kappa = \kappa_{q\omega}$ - $q\kappa_{\omega} = 0$ where q is the harmonic order, and $\kappa_{q\omega}$ and κ_{ω} are the generated radiation momentum and the driving laser momentum, respectively. The phase mismatch contribution can be found using independent terms given by[83,84]:

$$\Delta\kappa \approx q \cdot [\Delta\kappa_{geometric} + \Delta\kappa_{dispersive}] + \Delta\kappa_{dipole}, \tag{2.1}$$

where $\Delta\kappa_{geometric}$ is a geometric phase mismatch term that comes from the Gouy phase change across the driving laser focus; $\Delta\kappa_{dispersive}$ is a dispersive phase mismatch term due to the wavelength difference between the driving laser and the generated radiation which yields to a diphase caused by dispersion of the medium which is composed of neutral atoms and the ionised electrons (plasma) and $\Delta\kappa_{dipole}$ is the atomic dipole phase mismatch.

Assuming that the pulse propagating along the target, in the z-direction, has a Gaussian profile, the geometric term of the phase matching for high order harmonics (>500) is estimated as:

$$\Delta\kappa_{geometric} = \nabla\Phi_{Gouy} = \nabla(-arctan(z/z_R)) = -\frac{1}{1+(z/z_R)^2} \cdot \frac{1}{z_R}, \tag{2.2}$$

where z_R is the Rayleigh length which depends on the driving laser's central wavelength λ_0 and waist ω_0 by $z_R = \pi\omega_0^2/\lambda_0$. The dispersive term will depend on the number of neutral atoms and atoms that have been ionised by the pulse beam, and it is estimated as:

$$\Delta\kappa_{dispersive} \approx -P \cdot ([1-\eta] \cdot \Delta n \cdot 2\pi/\lambda_0 - \eta N_{atm} r_e \lambda_0), \tag{2.3}$$

where P is the pressure, η is the ionisation fraction, r_e is the classical electron radius, N_{atm} is the number density of atoms at 1 atm and Δn is the difference

between the refractive indexes of the neutral atoms at the driving laser and harmonic wavelengths. The dipole term is related to an intrinsic phase acquired by the electron during the HHG process. The phase is connected to the electron trajectory described by the electron after being ionised by the driving field and until it recombines with the pared ion. The electron trajectory depends on the intensity of the pulse. Within the strong field approximation (SFA)[35,85–87] using a single-atom response, the dipole phase is connected to a particular electron trajectory, and is calculated to be

$$\Delta\kappa_{dipole} \approx -\nabla(U_p \cdot (t_r(q\omega) - t_b(q\omega))), \tag{2.4}$$

where t_b and t_r are the birth and recombination times for the tunnel-ionised electron, respectively. Since the ponderomotive energy U_p is proportional to the intensity, shown in Eq.(1.2), the dipole phase is intensity dependent thus it varies across the interaction volume. The calculation does not include propagation effects such as self-phase modulation, plasma dephasing and absorption[88].

2.2 Macroscopic phase matching changes

The SXR yield generated via HHG is enhanced by iteratively optimising macroscopically phase matching parameters such as the gas pressure of the HHG target, the target position (z) with respect to the focal plane of the driving laser field and the opening of an iris placed 2 meters along the driving laser propagating beam before the HHG target. Here it is shown that the macroscopic variations of pressure and z-position lead to phase matching of specific energy ranges. These variations are associated with changes of specific phase-matching terms associated with a CEP phase change of the driving laser field. The changes in the SXR generation introduced by the iris opening are not studied in this thesis.

The highest HHG SXR yield, where phase matching is maximum, is achieved with a backing pressure of 8.7 bar which corresponds to a maximum pressure on the target of 7.4 bar and at a position z with respect to the focus defined here as z_{PM}. The experimental setup allows us to measure the absolute HHG target's z position with respect to the focal plane within a few mm precision being z_{PM} away from the driving focal plane (within 0 and 2 mm downstream (after the focal plane along the propagation direction)). However, relative positions can be measured with a high accuracy and reproducibility < 10 μm.

The SXR attosecond pulses are generated from the driving laser with a peak power of 0.45 PW/cm^2 which is not the maximum available power. A pellicle placed on the way of the driving laser pulse beam path reflects 13% of the energy

from the laser as shown in Fig. 1.10 in Sec. 1.3.2. The reduction of driving laser power used causes a decrease on the achieved cutoff photon energy from 550 eV to 450 eV. However, the spectral dependence on the phase matching terms is still preserved and studied here.

2.2.1 HHG target pressure dependence

With a fixed iris aperture and at a fixed z position z_{PM}, the helium gas pressure is varied around the phase matching pressure values $P_{PM} = 7.4$ bar from 4.6 bar to 8.4 bar in steps of 0.21 bar. These pressures are estimated values of the maximum pressures achieved at the HHG target which correspond to a backing pressure range from 5.5 bar to 10.0 bar with steps of 0.25 bar. From now on, pressure values should be assumed the maximum helium pressures estimated at the HHG target unless it is specifically stated otherwise. The detected SXR spectrum as a function of the estimated maximum pressure on the HHG target is shown in Fig. 2.1. The integration time used for each spectrum is 15 s.

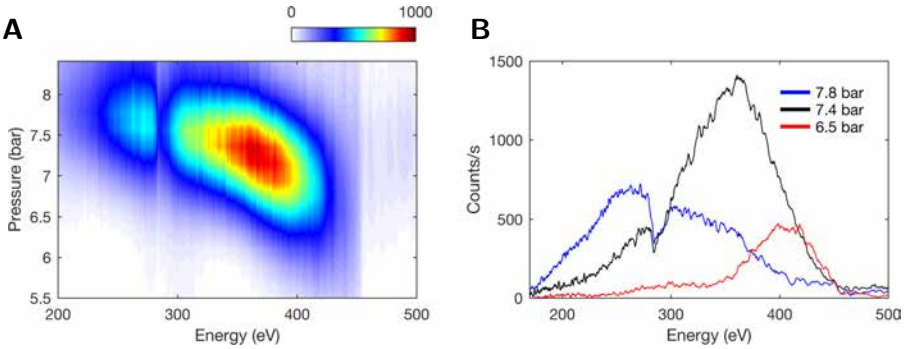

Fig. 2.1: SXR spectral pressure dependence. (**A**) Scan of the detected spectra as a function of the maximum pressure on the HHG target with pressure steps of 0.21 bar. (**B**) Spectral counts layouts from (A) at a given pressure. The phase matching pressure, from which the SXR yield is maximised, is found to be $P_{PM} = 7.4$ bar. Pressures above 8.4 bar and below 6 bar do not lead to an efficiently generated radiation. The detected radiation is integrated over 15 seconds. A titanium filter with a thickness of 200 nm is used to block the leftover part of the driving laser radiation from the HHG process. This metallic filter also blocks HHG radiation with photon energies above 454 eV.

SXR counts start significantly increasing at helium pressures above 6 bar until the maximum yield is produced at $P_{PM} = 7.4$ bar, the pressure at which the phase matching parameters are optimised for. Further increasing the pressure above P_{PM} leads to a decrease of the photon yield until being substantially suppressed at a pressure of 8.4 bar. Moreover, pressure variations give different generated spectral

ranges. Higher pressures lead to broaden spectra, i.e. at 7.8 bar the spectral intensity is maximum at 272 eV with a wide bandwidth of 150 eV at the FWHM, whilst at 7.4 bar the phase matched spectrum is much narrower with a 98 eV bandwidth and its maximum spectral intensity is moved towards higher energies at 364 eV. Further decreasing the pressure leads to even narrower spectra at higher energies. At 6.5 bar the spectrum has a bandwidth of 64 eV with the maximum spectral intensity found at 400 eV.

The shown spectra in Fig. 2.1 are measured using a titanium filter with a thickness of 200 nm which is placed along the SXR propagation direction to block the leftover of the driving laser. Since titanium has a strong absorption edge at 454 eV, radiation above 454 eV is highly suppressed. Figure 2.2 shows a similar pressure scan but using an aluminium filter to block the leftover driving laser radiation. Aluminium has a smoothed transmission across the entire water window, shown in Fig. 1.7. The integration time for each spectrum is set to 10 s. The backing pressure range is scanned from 6.0 to 10.0 bar with steps of 0.2 bar, which leads to a maximum pressure on the target from 5.0 to 8.4 bar with steps of 0.17 bar.

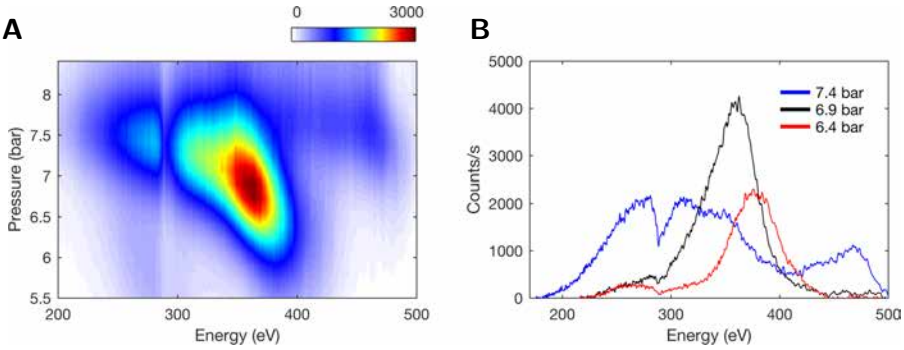

Fig. 2.2: SXR spectral pressure dependence with multi-half-cycle contribution. (**A**) Scan of the detected spectra as a function of the maximum pressure on the HHG target with pressure steps of 0.17 bar. (**B**) Spectral counts cross section from (A) at a given pressure. The phase matching pressure, from which the SXR yield is maximised, is found at $P_{PM} = 6.9$ bar. Pressures above 8 bar and below 5.5 bar do not lead to an efficiently generated radiation. The detected radiation is integrated over 10 seconds. An aluminium filter with a thickness of 100 nm is used to block the leftover driving laser radiation after the HHG process. This filter does not exhibit any absorption edge across the water window SXR region. At high pressures (7.4 bar), radiation from two consecutive half cycles is phase matched with photon energies above the titanium edge.

A very similar spectral dependence on pressure is found. Lower pressures phase match higher photon energies. An increase in pressure leads to a decrease of the generated photon energy while increasing the spectral bandwidth. The phase

matching pressure is found as $P_{PM} = 6.9$ bar with a maximum spectral intensity at 363 eV and a bandwidth of 63 eV at the FWHM. A higher pressure of 7.4 bar moves the maximum spectral intensity down to 281 eV with an extremely large bandwidth of 240 eV. A lower pressure of 6.4 bar has an even narrower spectrum than at a pressure of $P_{PM} = 6.9$ bar, with a bandwidth of 51 eV and a maximum spectral intensity at 376 eV. Small spectral differences between Figs. 2.1 and 2.2 come from the small differences in alignment and phase match conditions that differ day to day during the optimisation process of the SXR yield.

The spectral dip appearing at higher photon energies than the titanium edge when increasing pressures above P_{PM} can be assigned to the contribution of a consecutive half cycle of the driving laser pulse. A similar spectral half cycle contribution is found in Ref. Teichmann et al., 2016[40] with dependence on the driving laser field CEP. These spectral similarities between changing pressure and CEP drives us to study their analogous effect on the generated spectra via HHG. To simplify the comparison only the contribution of a single half cycle is taken into account, which corresponds to the spectra shown in Fig. 2.1.

2.2.2 HHG target position dependence

Another macroscopic parameter that controls the phase matching conditions is the position z of the HHG target with respect to the focal plane of the driving laser. Following the results shown in the previous section, using the optimised macroscopic phase matching parameters for enhancing the generated HHG yield given at a fixed iris aperture and fixed pressure $P_{PM} = 7.4$ bar, the z position is varied from z_{PM} - 0.350 mm to $z_{PM} + 0.175$ mm, from upstream to downstream, respectively, with steps of 25 μm. Figure 2.3 shows the spectral dependency on the z position of the HHG target with respect to the z_{PM}. The Rayleigh length of the driving laser is $z_R = 5.7$ mm which means that the z position is scanned with steps sizes of 0.4% of the z_R. The integration time for each recorded spectrum is 15 s.

The non-linear dependence of the generated spectrum with pressure, shown in Sec. 2.2.1, is again observed with respect to the z position dependence. At z_{PM} the yield is maximized with a 106 eV bandwidth at the FWHM with a maximum spectral intensity at 352 eV. Moving the HHG target upstream by 350 μm and downstream by 170 μm leads to bandwidths of 145 eV and 49 eV, respectively, and maximum spectral intensities at 321 eV and 408 eV, respectively. A titanium filter is placed on the SXR beam path to block the leftover of the driving laser field and also absorb radiation with energy above 450 eV, this limits the transmitted radiation to only come from a single half cycle of the driving laser field.

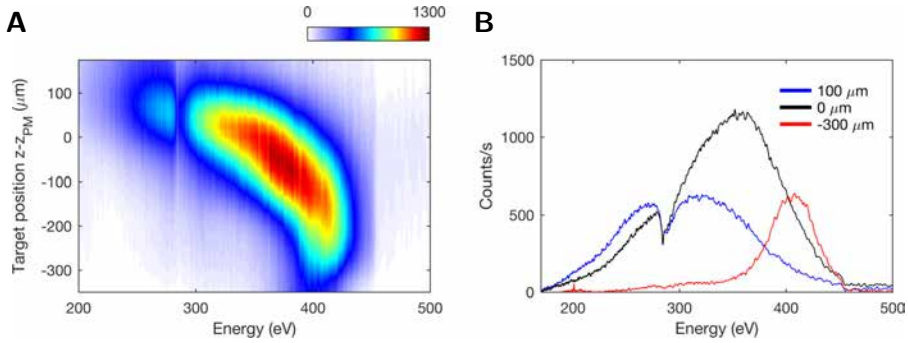

Fig. 2.3: SXR spectral z position dependence. (**A**) Scan of the detected spectra as a function of the HHG target z position respect to z_{PM} with position steps of 25 μm. (**B**) Spectral counts cross section from (A) at a given z position. An efficiently generated yield is found from -350 μm to 170 μm with respect to the z_{PM} position. The detected radiation is integrated over 15 seconds. A titanium filter with a thickness of 200 nm is used to block the leftover driving laser radiation after the HHG process. This metallic filter blocks radiation with photon energies above 454 eV limiting the radiation to come from a single half cycle of the driving laser.

The change of the z position and the gas pressure of the HHG target is analogous to a change of the driving electric field phase via an analysis of the phase matching conditions, as discussed in Sec. 2.3.

2.3 Phase matching position and pressure dependence

The changes of each of the phase mismatch terms are studied independently by integrating them in both time (over a half cycle of the driving laser field ($\pm$ 1.5 fs) at the maximum field intensity with zero CEP), and space (over 0.3 mm at the HHG target centre). Each phase mismatch term is associated with a phase by:

$$\phi_i = \frac{1}{n_z} \int_{z_{center}-0.15\ mm}^{z_{center}+0.15\ mm} \left(\frac{1}{n_t} \int_{-1.5fs}^{1.5fs} \Delta K_i(z,t) \cdot dt \right) \cdot dz, \tag{2.5}$$

where z_{center} is taken at the centre of the HHG target, and n_z and n_t are the number of samples taken in the propagation axis (z) and time (t), respectively. i refers to each of the phase matching contributing terms, dispersive, geometric and dipole. The total phase is calculated from the sum of each term. Only short trajectories are considered. Long trajectories are experimentally spatially suppressed due to propagation (more details are explained in Chap. 1, Sec. 1.2.2). For these phase matching calculations, the driving laser pulse is taken with a Gaussian spatio-temporal profile with a peak power of 0.45 PW/cm^2, waist of 54 μm and pulse

duration of 12 fs at the FWHM, centred at a wavelength of 1.85 μm. The pressure distribution across the HHG target is simulated in helium using a commercial computational fluid dynamics software and confirmed by an interferometric measurement, as shown in Chap. 1, Sec. 1.2.1. The HHG radiation is taken at 450 eV which matches the maximum cutoff energy achieved experimentally for a single half cycle contribution. Making the SXR monochromatic in the calculations has a negligible effect on the dispersive phase calculation but introduces a small error on the dipole phase contribution. The ϕ_{dipole} as a function of the HHG energy and the HHG target z position with respect to the driving laser focal plane are shown in Fig. 2.4. The total phase change introduced at different energies is also shown. Changing the HHG energy by 150 eV from 300 eV to 450 eV gives a discrepancy in the introduced phase of only 0.27 πrad. Neglecting this small absolute phase change introduced by the dipole intensity dependence simplifies the phase shift analysis as will now be discussed.

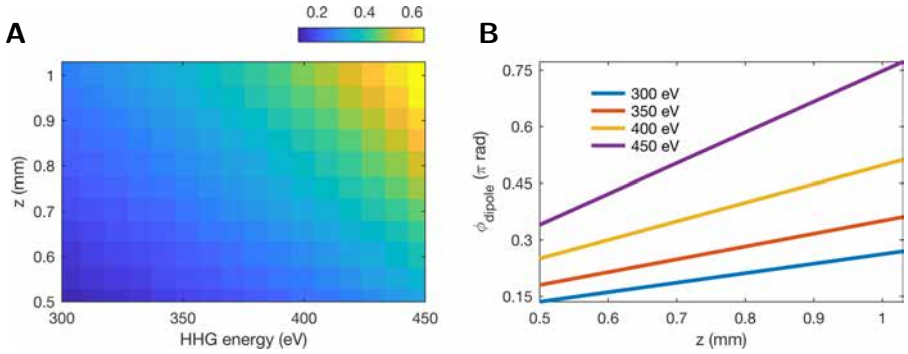

Fig. 2.4: ϕ_{dipole} dependence on the HHG target position and HHG photon energy. (**A**) Caculated ϕ_{dipole} (πrad) from a z position range downstream of the driving laser focal plane as a function of the generated HHG photon energy. (**B**) Cross section of the ϕ_{dipole} for given HHG photon energies as a function of the HHG target z position with respect to the driving focal plane. The absolute phase variation along the entire z position gives a discrepancy of 0.27 πrad from HHG photon energies at 300 eV with respect to 450 eV.

Figure 2.5 shows the calculated phase matching term contributions ϕ_i as a function of the maximum pressure on the HHG target and the z position of the HHG target with respect to the driving laser focal plane. Phase matching conditions from which the $\Delta\phi$ is minimised are found to be close to the driving laser focal plane between 0.5 and 1 mm downstream in the propagation direction. Having the HHG target position behind the focal plane is in agreement with what has been previously demonstrated in literature[29,79].

From Figs. 2.1 and 2.3 in Sec. 2.2 the maximum spectral intensity energy position as a function of the pressure on target and z position relative to z_{PM} are

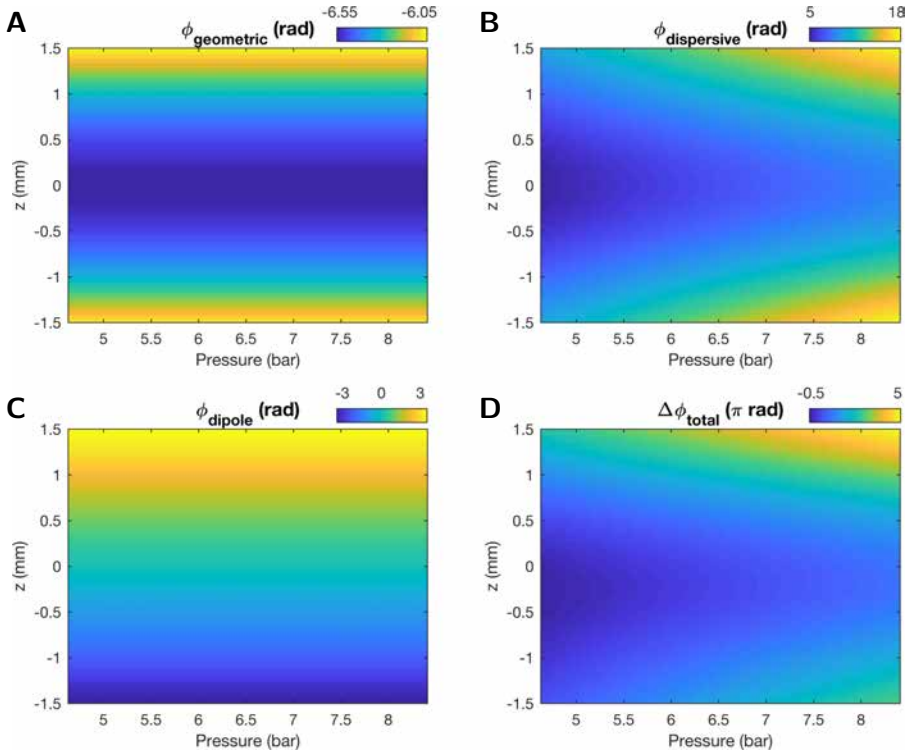

Fig. 2.5: Phase matching terms as a function of pressure and z position. (**A**) Geometric phase which is a Gouy phase contribution that is independent of pressure and changes sign across the focal plane. (**B**) Dispersive phase which is pressure and also intensity dependent since it depends on the ionisation fraction. (**C**) Dipole phase which is only intensity dependent. (**D**) Total phase calculated by the sum of (A), (B) and (C) phase contributions. Phase matching is achieved when the total phase is minimised which is found close to the focal plane downstream. z in mm refers to the propagation axis of the driving laser where $z = 0$ in the focal plane. Pressure in bar refers at the maximum pressure on the HHG target.

extracted and shown in Fig. 2.6.

From the analysis of the calculated phase, in Eq.(2.5), a change on pressure is also related to a change of the total phase. The same happens for a change in the z position. Since the absolute position of the target with respect to the driving laser focal plane is known to within a few mm, one can calculate at different absolute positions of the target which relates to the total phase change that is induced when changing the relative position and the pressure. It is found that at $z = 0.85$ mm downstream (after the focal plane), the phase change introduced by changing the z relative position matches with the phase change introduced by changing the pressure. These results are shown in Fig. 2.7.

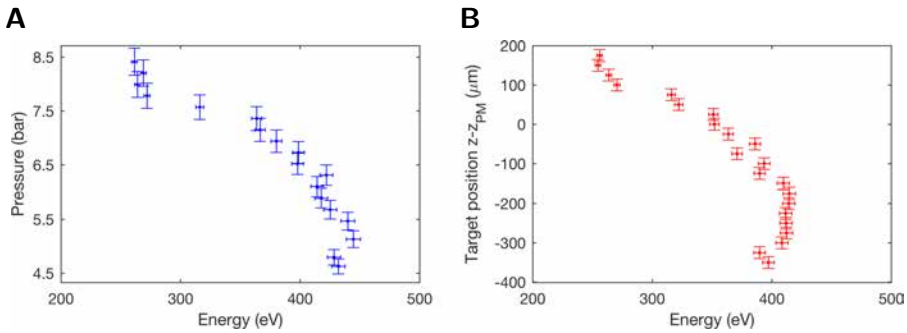

Fig. 2.6: Maximum spectral intensity shift as a function of macroscopic phase matching changes. (**A**) Pressure changes in the maximum pressure on the HHG target as a function of the spectral shifts, shown in Fig. 2.1. (**B**) Relative target position changes from z_{PM} as a function of the energy shifts, shown in Fig. 2.3.

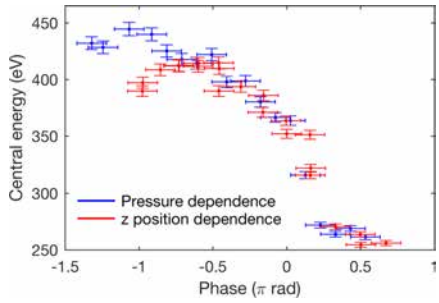

Fig. 2.7: Spectral central energy shift related to the calculated phase shift. Phase changes are related to spectral shifts introduced by both pressure changes on target at $z = 0.85$ mm HHG position downstream the focal plane of the driving laser, and relative target position changes at a pressure of $P_{PM} = 7.4$ bar.

Both phase variations from altering the pressure and the z position mainly come from variations in dispersion. This is obvious for a change in pressure since the geometric phase and the dipole phase do not depend on pressure and the only pressure dependent phase matching term is the dispersive phase. However, a shift in the z position causes a change in intensity and in Gouy phase causing all three phase matching terms to be varied. A change in the z position from 0.5 mm to 1 mm after the focal plane of the driving laser, only introduces a Gouy phase shift of 4% from the total phase variation. The dipole phase which is directly intensity dependent causes 26% of the total phase variation whereas the remaining 70% come from a variation of the dispersion due to a variation of the intensity dependent ionisation rate which varies the plasma density.

This phase shift can be compared with spectral cutoff energy shift introduced by actively tuning the CEP of the driving laser[40]. CEP changes affect the maximum

electric field amplitude that interacts with the atomic potential during the HHG process. Since the phase-matched energies are close to the cutoff, a change in the electric field amplitude yields a change in the generated SXR spectrum. The cutoff energy shift as a function of the CEP phase introduced a gradient of 125 eV/rad when only having contributions from a single half cycle. Here, the pressure and z position changes give a similar gradient of 140 eV/rad.

Recently it has been experimentally demonstrated that the extension of phase matching conditions changing from a loose to a tight focusing geometry caused the plasma-induced defocusing[79]. They used a loose focusing geometry with a 75 cm focal length and 1.2 mm gas cell, and compared this arrangement to a tight focusing geometry with 30 cm focal length with a 0.8 mm gas cell. The decrease of the driving laser refractive index on axis due to the generated plasma induces a defocusing effect similar to going through a divergent lens. This effect needs to be considered in tight focusing geometries resulting in the HHG radiation yield scaling by P^5 instead of P^2, when P is the pressure on the target. Figure 2.8 shows that in our regime the photon yield scales by $\approx P^5$ which according to literature indicates a regime where plasma defocusing should be considered.

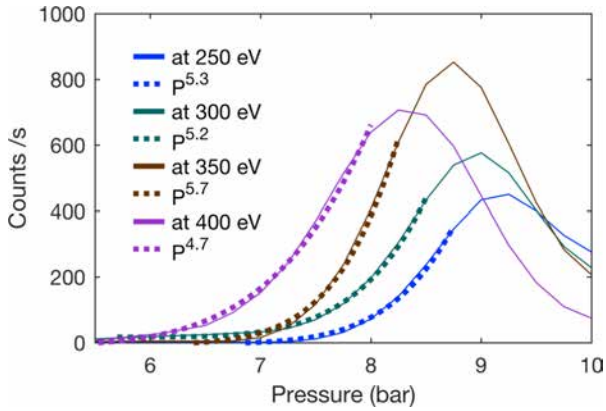

Fig. 2.8: Spectral photon yield scaling with pressure. SXR photon yield at a given energy (solid curves) as a function of pressure. These curves are fitted to a power function by Yield = A +(P - B)$^{\alpha}$ (dashed curves), where A, B and α are adjustable parameters and P is the pressure. The yield scaling with $\approx P^5$ gives indication of being in a tight focusing regime where plasma-defocusing has a relevant effect.

Simulations including the plasma-defocusing are executed by calculating the driving laser beam propagation along the HHG target for our experimental parameters. These simulations take into account non-linear effects that happen during the driving laser beam propagation such as absorption and self-phase modulation (space-time focusing and defocusing)[89,90]. The results show a maximum peak intensity found at 2 mm before the focusing plane (z = 0 mm). At z = 0Smm

the beam size reached its minimum value but the intensity is reduced due to a temporal broadening. Across 0.5 mm on the propagation direction (either centred at z = 0 mm (minimum waist) or at z = -2 mm where the intensity is maximised) the intensity changes by $< 3\%$, the waist changes by $< 1.5\%$ and the temporal broadening changes by $< 0.6\%$. This variation on the driving laser field parameters are negligible when being compared with both the dispersion and dipole phase changes. The simulations conclude that the non-linear propagation along our pressure gradient leads to an almost unperturbed propagated driving laser beam. Hence, although strong defocusing effects are expected due to the tight focusing geometry of the driving laser, the combination of wavelength, peak intensity and pressure distribution along the HHG target allows us to consider the driving laser field unperturbed. This time consuming and computationally costly simulations support the results found on the shown above simplified calculation of the phase matching.

2.4 Conclusion

The generated SXR radiation of the attosecond pulses can be tuned around 150 eV across the water window by changing either the z position of the HHG target with respect to the focal plane of the driving laser by 500 μm or the maximum pressure at the interaction region by 3.5 bar. Both macroscopic changes, pressure and z position, are associated with a phase matching change between the driving laser pulse and the generated HHG radiation. Simulations of the phase matching conditions show a clear variation of the plasma density when changing pressure, which is analogous to a gas density change, or when changing the z position, which is analogous to a change in intensity of the driving field, leading to a change on the ionisation fraction of the media. Moreover, the introduced phase shift is found to be equivalent to a CEP phase shift of the driving laser relating to 140 eV/rad and 125 eV/rad, respectively.

The driving laser focusing conditions are found to be in a tight focusing regime due to the SXR radiation yield increasing with $\approx P^5$. For this condition it has been demonstrated that plasma defocusing plays a significant role in phase matching[79]. However, extended simulations on the non-linear propagation of the driving laser field through the estimated pressure distribution in the HHG target show a close to unperturbed field along the propagation direction.

Tunable HHG source in the SXR regime are vital for the development of attosecond sources for user facilities which need spectral flexibility. All these results show that the phase matching parameters z, pressure and CEP are therefore linked

giving a complex multidimensional map of the SXR spectral output and that by correctly adjusting them one can select of the bandwidth and cutoff which can be tuned depending on the application. In fact, when optimising for a higher cutoff energy and a larger spectral bandwidth our standard procedure involves fine tuning each of these parameters for several iterations.

Creating attosecond pulses relies on the ability to obtain a broadband spectrum to support a short pulse in time and therefore the experimental results illustrate very well the crucial role that controlling the pressure, the target position and the CEP have in attosecond spectroscopy.